

Chapter 13

Standoff Distance and Depth Sectioning

Geometry Dependence of the Forward Operator

Chapter Focus: This extension develops the critical relationship between **source dimensionality** (0D, 1D, 2D, 3D) and the standoff-depth trade-off space. The forward operator \mathbf{G} has fundamentally different structures depending on source geometry, leading to different conditioning, reconstruction strategies, and multi-physics requirements.

Key Insight: The operator \mathbf{G} and reconstruction \mathcal{R} must be matched to source dimensionality D for optimal performance. Mismatch leads to severe Γ_{mm} penalties.

QFI Pipeline Position: $S(\mathbf{r}) \xrightarrow{\mathbf{G}(D)} F(\mathbf{r}) \xrightarrow{\mathcal{M}} D \xrightarrow{\mathcal{R}(D)} \hat{S}(\mathbf{r})$

Abbreviated Terms

Abbreviation	Definition	Abbreviation	Definition
CRB	Cramer–Rao Bound	FA	Failure Analysis
FFT	Fast Fourier Transform	FIM	Fisher Information Matrix
FOV	Field of View	IC	Integrated Circuit
NV	Nitrogen-Vacancy	PSF	Point Spread Function
QFI	Quantum Field Imaging	QFM	Quantum Field Metrology
Q-OTF	Quantum Optical Transfer Function	SNR	Signal-to-Noise Ratio
TIRF	Total Internal Reflection Fluorescence	TSV	Through-Silicon Via
0D	Zero-dimensional (point)	1D	One-dimensional (line)
2D	Two-dimensional (sheet)	3D	Three-dimensional (volume)
CAD	Computer-Aided Design	CS	Compressed Sensing
RIP	Restricted Isometry Property	κ	Condition number
D	Source dimensionality		

Abstract

This chapter addresses the critical relationship between standoff distance, depth sectioning capability, and reconstruction fidelity in Quantum Field Imaging (QFI) systems. The standoff distance—the gap between the quantum sensor (NV diamond) and the sample under test—fundamentally determines the spatial decay of the forward operator \mathbf{G} and, consequently, the conditioning of the inverse problem. We derive the exponential scaling of condition number with standoff, establish design rules for standoff tolerance, and quantify the impact of standoff errors on the model-mismatch penalty Γ_{mm} . The chapter then develops depth sectioning methodologies using multi-frequency deconvolution and multi-physics correlation, demonstrating how these techniques enable three-dimensional source localization from two-dimensional measurements. Calibration procedures for standoff determination complete the treatment, providing a practical foundation for production QFI systems.

13.1 Introduction: Why Standoff and Depth Matter

13.1.1 The Fundamental Challenge

In Quantum Field Imaging, the sensor plane (containing NV centers) is necessarily separated from the source plane (containing currents, thermal sources, or stress concentrations) by a standoff distance z_{standoff} . This separation is not merely a practical inconvenience—it fundamentally determines the information content of the measurement and the achievable reconstruction fidelity.

The physics is straightforward: fields decay with distance. A magnetic field from a current filament decays as $1/r^2$ in the near field and $1/r^3$ in the far field. A thermal perturbation diffuses and spreads. This decay is not uniform across spatial frequencies—high-frequency (fine-detail) information decays exponentially faster than low-frequency (coarse) information. The consequence is an increasingly ill-conditioned inverse problem as standoff increases.

Figure 13.1: Standoff Distance Geometry

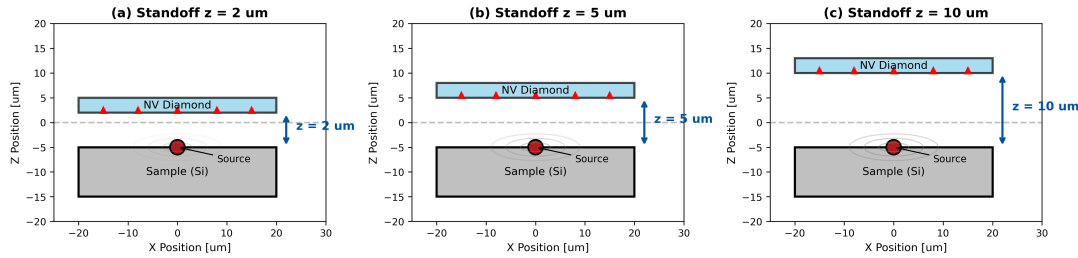


Figure 13.1: Standoff geometry in QFI. (a) Definition of standoff distance z_{standoff} between the NV sensor layer and the source plane. (b) The exponential decay of the Green's function kernel with spatial frequency k : $\tilde{G}(k) \propto e^{-|k|z_{\text{standoff}}}$. (c) Information loss at different standoff values, showing that fine spatial details are preferentially attenuated.

13.1.2 Historical Context

The standoff problem has deep roots in geophysics, where potential field methods (gravity, magnetics) face identical challenges. The seminal work of Parker in 1977 established that potential field inversion is fundamentally non-unique without prior constraints. The QFI context differs in several important ways:

1. **Controlled geometry:** Unlike geophysical surveys where sensor-source distance varies unpredictably, QFI systems can maintain precise standoff control through mechanical design.
2. **Multi-physics capability:** NV centers provide simultaneous access to magnetic, thermal, and strain fields, offering independent constraints that geophysical methods lack.
3. **Known source geometry:** In semiconductor FA applications, the permissible source volume is constrained by CAD data, dramatically reducing the solution space.

These differences transform an apparently intractable problem into a manageable one—but only with careful attention to standoff control and calibration.

13.1.3 Pain Points in Practice

Field experience with early QFI systems has identified standoff-related failures as the leading cause of reconstruction artifacts:

Table 13.1: Standoff-related pain points in QFI systems

Pain Point	Root Cause	Impact
Ghost sources	Incorrect standoff assumed in \mathbf{G}	False positives, depth errors
Resolution loss	Excessive standoff	Cannot resolve sub-10 μm features
Depth-amplitude ambiguity	Single-physics measurement	Cannot distinguish deep-strong from shallow-weak
Calibration drift	Thermal/mechanical instability	Time-varying Γ_{mm} degradation
Sample tilt	Non-parallel sensor-sample planes	Spatially varying z_{standoff}

13.1.4 Chapter Objectives and Figures of Merit

This chapter provides the theoretical foundation and practical methods to address these challenges. The key figures of merit are:

Table 13.2: Key figures of merit for standoff and depth sectioning

Figure of Merit	Symbol	Target	Units
Standoff distance	z_{standoff}	< 10	μm
Standoff error	$\varepsilon_{\text{standoff}}$	< 5%	—
Standoff stability	$\sigma_z/z_{\text{standoff}}$	< 1%	—
Condition number	$\kappa(\mathbf{G})$	< 10^4	—
Model-mismatch penalty	Γ_{mm}	> 0.95	—
Depth resolution	δz	< 5	μm

13.1.5 Notation and Symbols

Table 13.3 summarizes the principal symbols used throughout this chapter.

Table 13.3: Principal notation for Chapter 13

Symbol	Definition	Units
h, z_{standoff}	Standoff distance (sensor-to-source)	μm
Δx	Lateral sampling pitch / target resolution	μm
k_{\min}, k_{\max}	Minimum / maximum spatial frequency	μm^{-1}
$\kappa(\mathbf{G})$	Condition number of forward operator	dimensionless
Γ_{mm}	Model-mismatch penalty factor ($0 \leq \Gamma_{\text{mm}} \leq 1$)	dimensionless
Γ_{inv}	Inversion fidelity ($0 \leq \Gamma_{\text{inv}} \leq 1$)	dimensionless
$\varepsilon_{\text{standoff}}$	Normalized standoff error	dimensionless
$\langle k^2 \rangle$	Mean-square spatial frequency of source	μm^{-2}
D	Source dimensionality (0, 1, 2, or 3)	dimensionless
K	Number of non-zero (sparse) source elements	dimensionless
N	Total number of unknowns in discretized problem	dimensionless
$\delta(f)$	Skin depth at frequency f	μm
k_B, k_T	Effective spatial-frequency decay constants (magnetic, thermal)	μm^{-1}
Φ_{multi}	Multi-physics correlation factor	dimensionless

13.2 Physics of Standoff Distance

13.2.1 The Forward Operator in Fourier Space

The forward operator \mathbf{G} maps the source distribution $S(\mathbf{r})$ to the measured field $F(\mathbf{r}')$ at the sensor plane. For a planar geometry where the sensor plane is at $z = 0$ and sources are located at $z = -z_{\text{standoff}}$, the relationship in Fourier space takes a particularly elegant form.

Theorem 13.2.1 (Fourier-Domain Forward Operator). *For a source $S(x, y)$ at depth z_{standoff} below a planar sensor, the measured magnetic field component $B_z(x, y)$ satisfies:*

$$\tilde{B}_z(k_x, k_y) = \tilde{G}(k_x, k_y; z_{\text{standoff}}) \cdot \tilde{J}(k_x, k_y) \quad (13.1)$$

where the Green's function kernel is:

$$\tilde{G}(k; z_{\text{standoff}}) = \frac{\mu_0}{2} e^{-|k|z_{\text{standoff}}}, \quad k = \sqrt{k_x^2 + k_y^2} \quad (13.2)$$

Proof. Starting from the Biot-Savart law in integral form and taking the 2D Fourier transform with respect to (x, y) , the convolution in real space becomes multiplication in Fourier space. The z -dependence enters through the vertical separation, yielding the exponential decay factor. \square

$$\tilde{G}(k; z_{\text{standoff}}) = \frac{\mu_0}{2} e^{-|k|z_{\text{standoff}}} \quad (13.3)$$

This exponential decay is the fundamental source of ill-conditioning in QFI reconstruction. High spatial frequencies (large $|k|$) are exponentially suppressed relative to low frequencies.

13.2.2 Condition Number Scaling

The condition number $\kappa(\mathbf{G})$ of the discretized forward operator quantifies the amplification of measurement noise into reconstruction error. For the Biot-Savart kernel, this scaling is exponential.

Theorem 13.2.2 (Condition Number Scaling with Standoff). *For a 2D Biot-Savart forward model with spatial frequency range $[k_{\min}, k_{\max}]$ and standoff z_{standoff} , the condition number scales as:*

$$\kappa(\mathbf{G}) = \frac{\sigma_{\max}}{\sigma_{\min}} = e^{(k_{\max} - k_{\min})z_{\text{standoff}}} \approx e^{k_{\max}z_{\text{standoff}}} \quad (13.4)$$

where the approximation holds when $k_{\min} \ll k_{\max}$.

Proof. In Fourier space, the forward operator is diagonal with entries $\tilde{G}(k) = \frac{\mu_0}{2} e^{-|k|z_{\text{standoff}}}$. The singular values are the absolute values of these diagonal entries. Therefore:

$$\sigma_{\max} = |\tilde{G}(k_{\min})| = \frac{\mu_0}{2} e^{-k_{\min}z_{\text{standoff}}} \quad (13.5)$$

$$\sigma_{\min} = |\tilde{G}(k_{\max})| = \frac{\mu_0}{2} e^{-k_{\max}z_{\text{standoff}}} \quad (13.6)$$

The condition number follows directly:

$$\kappa(\mathbf{G}) = \frac{e^{-k_{\min}z_{\text{standoff}}}}{e^{-k_{\max}z_{\text{standoff}}}} = e^{(k_{\max} - k_{\min})z_{\text{standoff}}} \quad (13.7)$$

\square

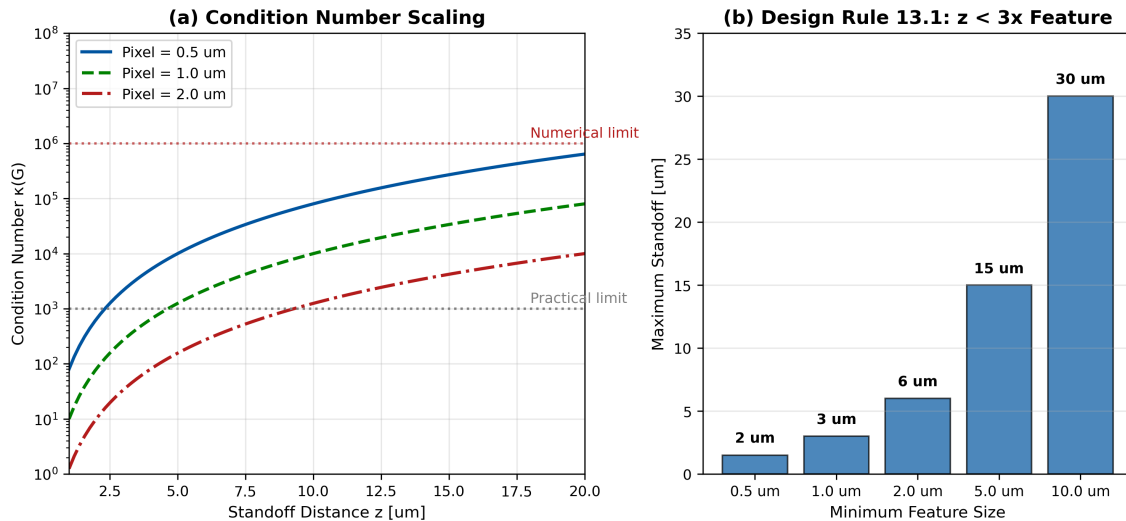


Figure 13.2: Condition number scaling with standoff distance. (a) Log-linear plot of $\kappa(\mathbf{G})$ vs. z_{standoff} for different spatial resolutions Δx . (b) Contour plot of $\kappa(\mathbf{G})$ in the $(z_{\text{standoff}}, \Delta x)$ plane with $\kappa = 10^4$ stability boundary marked. (c) Practical operating regions for different applications.

13.2.3 The Standoff-Resolution Trade-off

The exponential condition number scaling establishes a fundamental trade-off between standoff distance and achievable resolution.

Corollary 13.2.1 (Maximum Standoff for Stable Reconstruction). *For stable reconstruction with $\kappa(\mathbf{G}) < \kappa_{\max}$, the standoff must satisfy:*

$$z_{\text{standoff}} < \frac{\ln(\kappa_{\max})}{k_{\max}} = \frac{\ln(\kappa_{\max}) \cdot \Delta x}{\pi} \quad (13.8)$$

where $k_{\max} = \pi/\Delta x$ for Nyquist-limited sampling at grid spacing Δx .

For stable reconstruction with condition number $\kappa < 10^4$, the standoff must satisfy:

$$z_{\text{standoff}} < 3\Delta x \quad (13.9)$$

To resolve 1 μm features, require $z_{\text{standoff}} < 3 \mu\text{m}$. This is the “3×” rule for QFI system design.

Remark 13.2.1 (Validity of the 3× Rule). Design Rule 13.2.1 assumes:

1. **Fourier-diagonal forward model:** The source–sensor geometry is translationally invariant (planar, infinite extent), so \mathbf{G} diagonalizes in Fourier space.
2. **Nyquist-limited bandwidth:** $k_{\max} = \pi/\Delta x$, i.e., the sampling grid sets the maximum recoverable spatial frequency.
3. **$\kappa < 10^4$ stability threshold:** This is an empirical guideline; specific applications may tolerate higher or require lower κ .

Failure modes: The rule becomes inaccurate for (i) finite field-of-view effects (edge artifacts modify effective k_{\min}); (ii) non-planar sensor surfaces (tilt, curvature); (iii) vector-field components with different spatial-frequency weighting; (iv) non-uniform NV depth distribution broadening the effective standoff.

Example 13.2.1 (Standoff Budget for IC Failure Analysis). Consider a QFI system designed for IC failure analysis with target resolution $\Delta x = 2 \mu\text{m}$ and acceptable condition number $\kappa_{\max} = 10^3$.

Given:

- Target resolution: $\Delta x = 2 \mu\text{m}$
- Maximum condition number: $\kappa_{\max} = 1000$

Solution: The maximum spatial frequency is $k_{\max} = \pi/\Delta x = \pi/(2 \times 10^{-6} \text{ m}) = 1.57 \times 10^6 \text{ m}^{-1}$.

The maximum standoff is:

$$z_{\text{standoff}}^{\max} = \frac{\ln(1000)}{1.57 \times 10^6 \text{ m}^{-1}} = \frac{6.91}{1.57 \times 10^6 \text{ m}^{-1}} = 4.4 \mu\text{m} \quad (13.10)$$

Practical allocation:

- NV layer depth in diamond: $0.02 \mu\text{m}$
- Air gap (minimum): $1.0 \mu\text{m}$
- IC passivation: $2.0 \mu\text{m}$
- Metal layer depth: $1.0 \mu\text{m}$
- Total: $4.02 \mu\text{m} < 4.4 \mu\text{m} \checkmark$

The design is feasible with minimal margin.

13.3 Standoff Error and Model-Mismatch Penalty

13.3.1 The Model-Mismatch Framework

When the assumed standoff $z_{\text{standoff}}^{\text{model}}$ differs from the true standoff $z_{\text{standoff}}^{\text{true}}$, the reconstruction uses an incorrect forward model. This model mismatch degrades reconstruction fidelity through the penalty factor Γ_{mm} .

Definition 13.3.1 (Standoff Error). The normalized standoff error is:

$$\varepsilon_{\text{standoff}} = \frac{|z_{\text{standoff}}^{\text{model}} - z_{\text{standoff}}^{\text{true}}|}{z_{\text{standoff}}^{\text{true}}} \quad (13.11)$$

Theorem 13.3.1 (Standoff Contribution to Γ_{mm}). *For small standoff errors $\varepsilon_{\text{standoff}} \ll 1$, the contribution to the model-mismatch penalty is:*

$$\Gamma_{\text{mm}}^{\text{standoff}} \approx 1 - \varepsilon_{\text{standoff}}^2 \cdot \langle k^2 \rangle \cdot z_{\text{standoff}}^2 \quad (13.12)$$

where $\langle k^2 \rangle$ is the mean-square spatial frequency of the source.

Proof. The model mismatch creates a multiplicative error in Fourier space:

$$\frac{\tilde{G}(k; z_{\text{standoff}}^{\text{model}})}{\tilde{G}(k; z_{\text{standoff}}^{\text{true}})} = e^{-k(z_{\text{standoff}}^{\text{model}} - z_{\text{standoff}}^{\text{true}})} = e^{-k \cdot \delta z} \quad (13.13)$$

where $\delta z = z_{\text{standoff}}^{\text{model}} - z_{\text{standoff}}^{\text{true}}$.

For small δz , Taylor expansion gives:

$$e^{-k\delta z} \approx 1 - k\delta z + \frac{(k\delta z)^2}{2} \quad (13.14)$$

The mean-square error averaged over the source spectrum is:

$$\text{MSE} \approx \langle k^2 \rangle \cdot \delta z^2 = \langle k^2 \rangle \cdot z_{\text{standoff}}^2 \cdot \varepsilon_{\text{standoff}}^2 \quad (13.15)$$

Since $\Gamma_{\text{mm}} \approx 1 - \text{MSE}$ for small errors, the result follows. \square

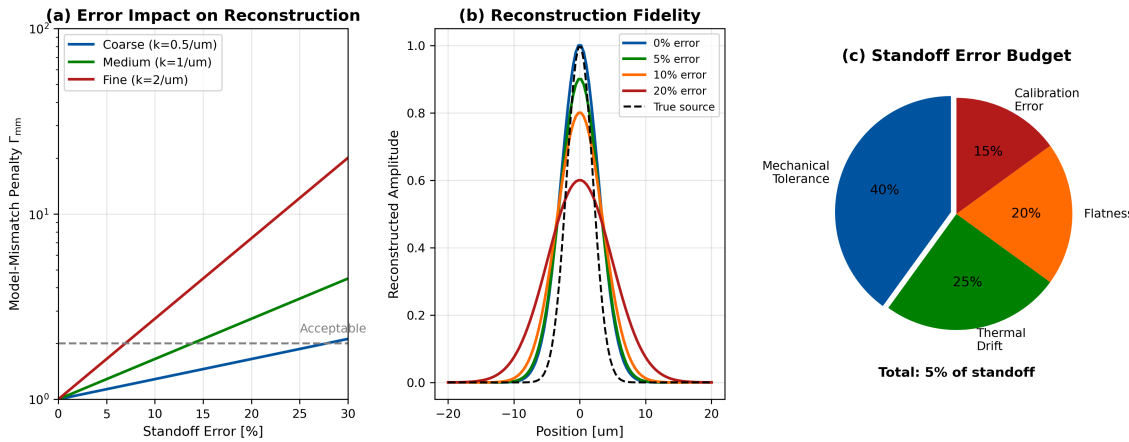


Figure 13.3: Impact of standoff error on reconstruction. (a) Γ_{mm} vs. $\varepsilon_{\text{standoff}}$ for different source spatial frequencies. (b) Reconstruction error maps showing ghost artifacts from 5% standoff error. (c) Sensitivity analysis: $\partial\Gamma_{\text{mm}}/\partial\varepsilon_{\text{standoff}}$ as a function of source depth.

13.3.2 Quantitative Standoff Tolerance

To maintain $\Gamma_{\text{mm}} > 0.95$, the standoff error must satisfy:

$$\varepsilon_{\text{standoff}} < \frac{0.22}{\sqrt{\langle k^2 \rangle} \cdot z_{\text{standoff}}} \quad (13.16)$$

For typical IC sources with feature size $\sim 1 \mu\text{m}$ ($\sqrt{\langle k^2 \rangle} \approx 3 \mu\text{m}^{-1}$) and $z_{\text{standoff}} = 5 \mu\text{m}$:

$$\varepsilon_{\text{standoff}} < 1.5\% \quad (13.17)$$

This corresponds to $\delta z < 75 \text{ nm}$ absolute tolerance.

Remark 13.3.1 (Validity of Standoff Tolerance Specification). The tolerance formula (Eq. 13.16) assumes:

1. **Small error:** $\varepsilon_{\text{standoff}} \ll 1$ (first-order Taylor expansion of the exponential kernel).
2. **Known source spectrum:** The mean-square spatial frequency $\langle k^2 \rangle$ is either known *a priori* or estimated from the measured data (e.g., via power spectral density of the field map).
3. **Uniform standoff error:** The standoff error is spatially constant across the FOV; spatially varying errors (tilt, topography) require the local treatment of Section 13.6.3.

For errors exceeding $\varepsilon > 0.2$, the quadratic approximation breaks down and full numerical simulation of Γ_{mm} is recommended.

13.3.3 Sources of Standoff Error

Table 13.4: Sources of standoff error and mitigation strategies

Error Source	Typical Magnitude	Character	Mitigation
NV depth variation	$\pm 5 \text{ nm}$	Systematic, wafer-scale	Delta-doping process control
Diamond surface roughness	1 nm RMS	Random, local	Polishing specification
Air gap control	$\pm 0.5 \mu\text{m}$	Systematic	Kinematic mount, interferometry
IC topography	0–5 μm	Systematic, patterned	Index-matching fluid, CAD correction
Sample tilt	$\pm 0.1^\circ$	Systematic, linear	Auto-leveling stage
Thermal expansion	10 nm K^{-1}	Time-varying	Temperature stabilization

Example 13.3.1 (Standoff Error Budget). Construct a standoff error budget for a production QFI system with $z_{\text{standoff}} = 5 \mu\text{m}$ target and $\varepsilon_{\text{standoff}} < 2\%$ requirement ($\delta z < 100 \text{ nm}$).

Error allocation:

Source	Allocation	$\delta z^2 (\text{nm}^2)$
NV depth uncertainty	10 nm	100
Diamond surface	5 nm	25
Air gap control	50 nm	2500
IC topography (corrected)	30 nm	900
Tilt (over 100 μm FOV)	17 nm	289
Thermal drift	20 nm	400
RSS Total		4214
δz_{total}	65 nm	—
$\varepsilon_{\text{standoff}}$	1.3%	< 2% ✓

The design meets specification with 35% margin.

13.4 Quantum State Channels for Depth Sectioning

A defining feature of quantum field imaging is that the sensor comprises multiple *quantum state channels*—distinct quantum degrees of freedom that each provide independent information about the source. For NV centers, these channels include the four crystallographic orientations, multiple spin transitions, and coherence orders accessible through different pulse sequences. This section develops the theoretical framework for exploiting these quantum channels to enhance depth sectioning beyond classical limits.

13.4.1 The Multi-Channel Quantum Sensor

Definition 13.4.1 (Quantum State Channel). A quantum state channel \mathcal{Q}_i is a distinct quantum degree of freedom that transduces a physical field $F(\mathbf{r})$ into a measurable signal S_i through

a channel-specific transfer function:

$$S_i = \int G_i(\mathbf{r}, \mathbf{r}'; z) \cdot F(\mathbf{r}') d^3 r' \quad (13.18)$$

where G_i depends on the quantum state properties (orientation, transition, coherence time).

For NV centers in diamond, the available quantum state channels are:

Table 13.5: Quantum state channels in NV-based QFI

Channel Type	Number	Physical Basis	Depth Information
NV orientations	4	Tetrahedral axes $\{\hat{n}_i\}$	Vector projection
Spin transitions	2	$m_s : 0 \leftrightarrow \pm 1$	Zeeman splitting
Coherence orders	3+	T_2^*, T_2, T_1	Noise spectroscopy
AC frequencies	Continuous	Pulse sequence filter	Skin depth selection

13.4.2 Four-Axis Vector Reconstruction

The four NV orientations in diamond point along the $\langle 111 \rangle$ crystallographic directions, forming a tetrahedral geometry:

$$\hat{n}_1 = \frac{1}{\sqrt{3}}(1, 1, 1) \quad \hat{n}_2 = \frac{1}{\sqrt{3}}(1, -1, -1) \quad (13.19)$$

$$\hat{n}_3 = \frac{1}{\sqrt{3}}(-1, 1, -1) \quad \hat{n}_4 = \frac{1}{\sqrt{3}}(-1, -1, 1) \quad (13.20)$$

Each axis measures the projection of the magnetic field:

$$\Delta u_i = \gamma_{\text{NV}}(\hat{n}_i \cdot \vec{B}) = \gamma_{\text{NV}}(n_{ix}B_x + n_{iy}B_y + n_{iz}B_z) \quad (13.21)$$

where $\gamma_{\text{NV}} = 28 \text{ GHz T}^{-1}$ is the NV gyromagnetic ratio.

Theorem 13.4.1 (Vector Reconstruction from Four Axes). *Given measurements $\{\Delta u_1, \Delta u_2, \Delta u_3, \Delta u_4\}$ from four NV orientations, the full magnetic field vector is:*

$$\vec{B} = \frac{1}{\gamma_{\text{NV}}} \mathbf{N}^{-1} \begin{pmatrix} \Delta u_1 \\ \Delta u_2 \\ \Delta u_3 \\ \Delta u_4 \end{pmatrix} \quad (13.22)$$

where $\mathbf{N} = [\hat{n}_1, \hat{n}_2, \hat{n}_3, \hat{n}_4]^T$ is the 4×3 orientation matrix. The system is overdetermined, and the least-squares solution provides noise rejection.

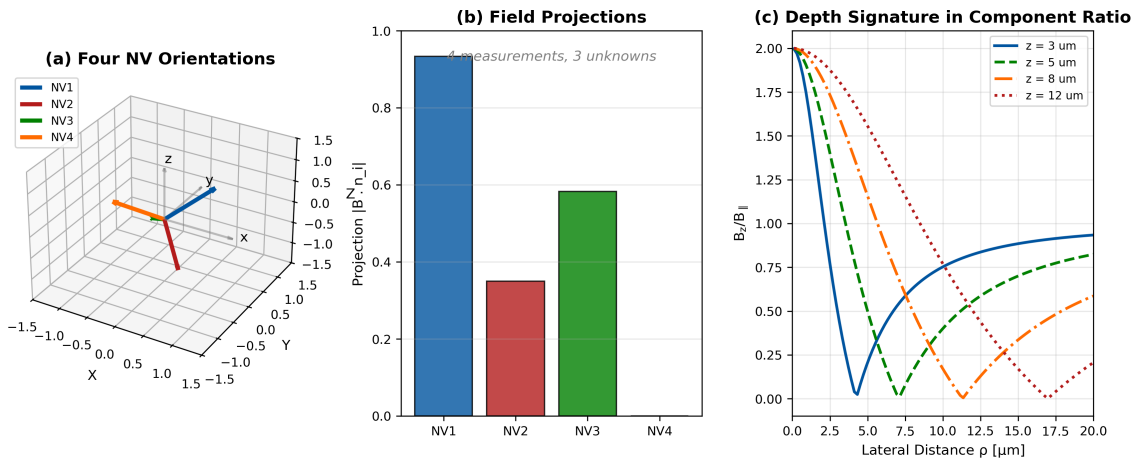


Figure 13.4: Four-axis NV geometry for vector reconstruction. (a) Tetrahedral arrangement of NV axes in diamond lattice. (b) Projection of a magnetic field vector onto each axis. (c) Depth-dependent sensitivity: different axes have varying sensitivity to sources at different lateral positions. (d) Redundancy enables noise rejection and consistency checks.

13.4.2.1 Depth Information from Vector Components

The key insight is that the *ratio* of field components carries depth information independent of source amplitude:

$$\frac{B_z}{B_{\parallel}} = \frac{B_z}{\sqrt{B_x^2 + B_y^2}} = f(z, \rho) \quad (13.23)$$

where ρ is the lateral distance from source to measurement point.

Consider an infinite straight wire carrying current I along \hat{y} , located at depth z below the sensor plane. Using the Biot–Savart law in the coordinate system where the measurement point is at $(x, 0, 0)$ and the wire is at $(0, 0, -z)$, the field components at lateral offset $\rho = |x|$ are:

$$B_z(\rho, z) = \frac{\mu_0 I}{2\pi} \cdot \frac{\rho}{\rho^2 + z^2}, \quad (13.24)$$

$$B_{\parallel}(\rho, z) = \frac{\mu_0 I}{2\pi} \cdot \frac{z}{\rho^2 + z^2}. \quad (13.25)$$

The ratio is therefore:

$$\boxed{\frac{B_z}{B_{\parallel}} = \frac{\rho}{z}} \quad (13.26)$$

This ratio is independent of source amplitude I and distance $r = \sqrt{\rho^2 + z^2}$, providing a depth estimate that is *immune to the depth–amplitude ambiguity* that plagues scalar measurements. Equivalently, $z = \rho \cdot B_{\parallel}/B_z$.

Remark 13.4.1. The ratio $B_z/B_{\parallel} = \rho/z$ means that directly above the wire ($\rho \rightarrow 0$), the field is purely in-plane ($B_z/B_{\parallel} \rightarrow 0$), while far from the wire ($\rho \gg z$), the field becomes predominantly out-of-plane ($B_z/B_{\parallel} \rightarrow \infty$). The crossover at $\rho = z$ identifies the depth. For geometries other than an infinite wire (e.g., finite segments, current loops), the functional form of $f(z, \rho)$ changes, but the principle that amplitude-independent ratios encode depth remains valid.

Use the B_z/B_{\parallel} ratio for depth estimation when source amplitude is unknown. From Eq. (13.26):

$$z = \rho \cdot \frac{B_{\parallel}}{B_z} \quad (13.27)$$

The depth uncertainty follows from error propagation:

$$\frac{\delta z}{z} \approx \sqrt{\left(\frac{\sigma_{B_z}}{B_z}\right)^2 + \left(\frac{\sigma_{B_{\parallel}}}{B_{\parallel}}\right)^2} \quad (13.28)$$

For typical 5% component uncertainties: $\delta z/z \approx 7\%$.

Validity conditions: Assumes (i) a wire-like source geometry where B_z and B_{\parallel} have the stated functional forms; (ii) measurement at a point where ρ is known or can be estimated from the field map; (iii) single dominant source (superposition of multiple sources complicates the ratio interpretation).

13.4.3 State-Dependent Transfer Functions

Each quantum state channel has a distinct transfer function that depends on both the geometric projection and the quantum coherence properties.

Definition 13.4.2 (Quantum Transfer Function). The quantum transfer function for channel i is:

$$\tilde{G}_{Q,i}(k; z) = \underbrace{\tilde{G}_{\text{geo}}(k; z)}_{\text{Geometric}} \times \underbrace{(\hat{n}_i \cdot \hat{e}_B)}_{\text{Projection}} \times \underbrace{H_i(\omega)}_{\text{Quantum filter}} \quad (13.29)$$

where:

- $\tilde{G}_{\text{geo}}(k; z) = e^{-|k|z}$ is the geometric decay
- $\hat{n}_i \cdot \hat{e}_B$ is the projection onto axis i
- $H_i(\omega)$ is the frequency response of the pulse sequence

The quantum filter function $H_i(\omega)$ depends on the measurement protocol:

Table 13.6: Quantum filter functions for different protocols

Protocol	$H(\omega)$	Bandwidth
Ramsey (DC)	$\text{sinc}^2(\omega T_2^*/2)$	$\sim 1/T_2^*$
Spin echo (AC)	$\text{sinc}^2(\omega\tau - \pi/2)$	$\sim 1/\tau$
CPMG- N	Comb at $\omega = \pi/\tau$	$\sim 1/(N\tau)$
XY-8	Narrow band at ω_0	$\sim 1/(8N\tau)$

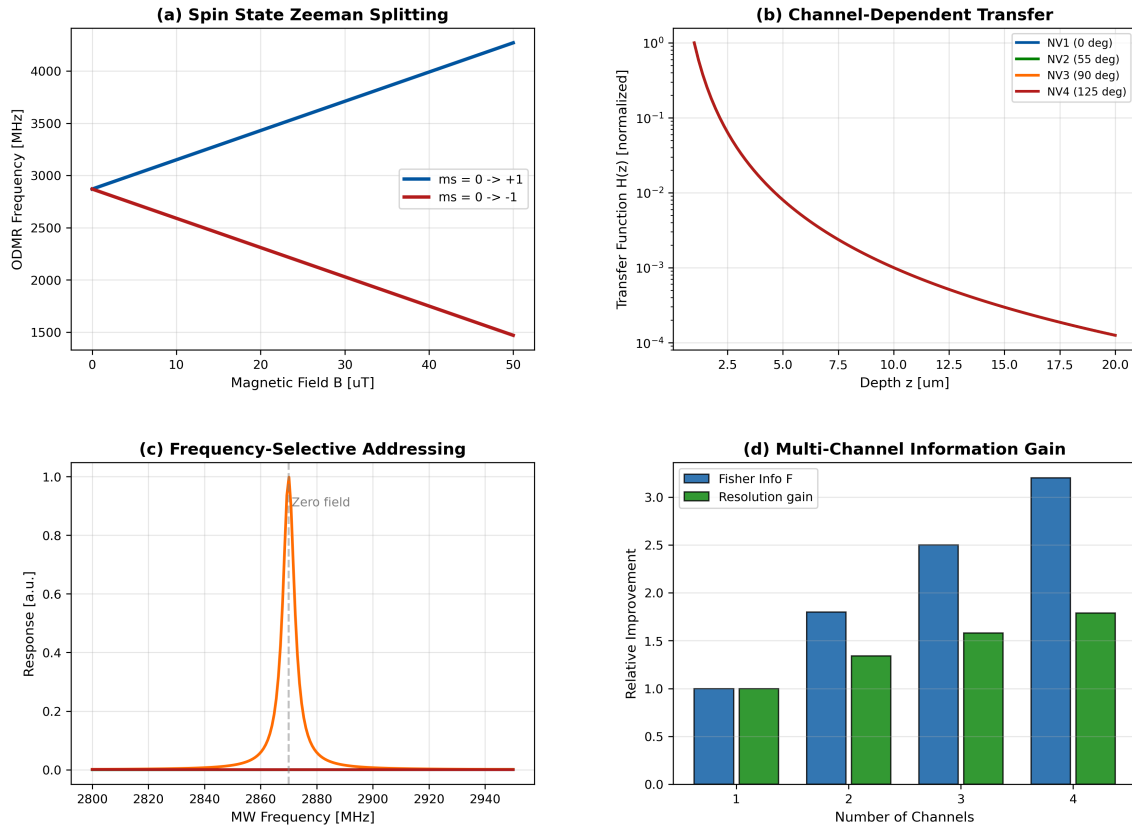


Figure 13.5: State-dependent quantum transfer functions. (a) Geometric transfer function $\tilde{G}_{\text{geo}}(k, z)$ showing exponential decay with depth. (b) Quantum filter functions $H(\omega)$ for different pulse sequences. (c) Combined transfer function $\tilde{G}_Q = \tilde{G}_{\text{geo}} \times H$ showing frequency-selective depth sensitivity. (d) Information content vs. frequency for sources at different depths.

13.4.4 AC Magnetometry for Depth Profiling

A powerful technique for depth sectioning exploits the *skin effect*: AC currents at frequency f penetrate conductors only to a characteristic depth $\delta(f)$.

Theorem 13.4.2 (Skin Depth Formula). *For a conductor with resistivity ρ and permeability μ :*

$$\delta(f) = \sqrt{\frac{\rho}{\pi\mu f}} \quad (13.30)$$

By driving the sample with AC current at frequency f and using synchronized pulse sequences to detect $B(f)$, the measurement selectively probes currents within depth $\sim \delta(f)$ of the conductor surface. In IC failure analysis, the relevant conductors are the metal interconnect layers (Cu, Al, W); the silicon substrate has resistivity orders of magnitude higher than metals, giving skin depths in the metre range at kHz frequencies, so the skin effect in lightly doped Si is negligible for practical depth profiling.

Table 13.7: Skin depth in IC-relevant conductors at various frequencies. Silicon is included for reference; its large skin depth confirms that the skin effect plays no practical role in lightly doped Si substrates.

Frequency	Cu ($\rho = 1.7 \mu\Omega\cdot\text{cm}$)	Al ($\rho = 2.7 \mu\Omega\cdot\text{cm}$)	W ($\rho = 5.3 \mu\Omega\cdot\text{cm}$)	Si [†] ($\rho = 1 \Omega\cdot\text{cm}$)
1 kHz	2.1 mm	2.6 mm	3.7 mm	1.6 m
100 kHz	210 μm	260 μm	370 μm	16 cm
10 MHz	21 μm	26 μm	37 μm	1.6 cm
1 GHz	2.1 μm	2.6 μm	3.7 μm	1.6 mm

[†]Lightly doped Si ($\rho = 1 \Omega\cdot\text{cm}$, $\mu = \mu_0$). Heavily doped Si ($\rho \sim 10^{-3} \Omega\cdot\text{cm}$) gives skin depths $\sim 30\times$ smaller. Values computed via $\delta = \sqrt{\rho/(\pi\mu_0 f)}$.

Implication for QFI depth profiling: AC magnetometry depth sectioning exploits the skin effect *in the metal conductors* of the IC, not in the silicon substrate. By sweeping the drive frequency, current is confined to progressively shallower metal layers. Depth profiling of currents in lightly doped Si requires alternative approaches such as multi-physics correlation (Section 13.5.3).

Algorithm: Frequency-Sweep Depth Profiling

1. Select frequency set $\{f_1, f_2, \dots, f_N\}$ spanning target depth range
2. For each f_n :
 - (a) Drive sample with AC current at frequency f_n
 - (b) Configure pulse sequence for narrowband detection at f_n
 - (c) Acquire magnetic field map $B_n(x, y)$
3. Construct depth-resolved current density $J(x, y, z)$ by deconvolution:

$$J(x, y, z) \approx \sum_n w_n(z) \cdot J_n(x, y) \quad (13.31)$$

where $w_n(z)$ are depth-weighting kernels derived from skin depth

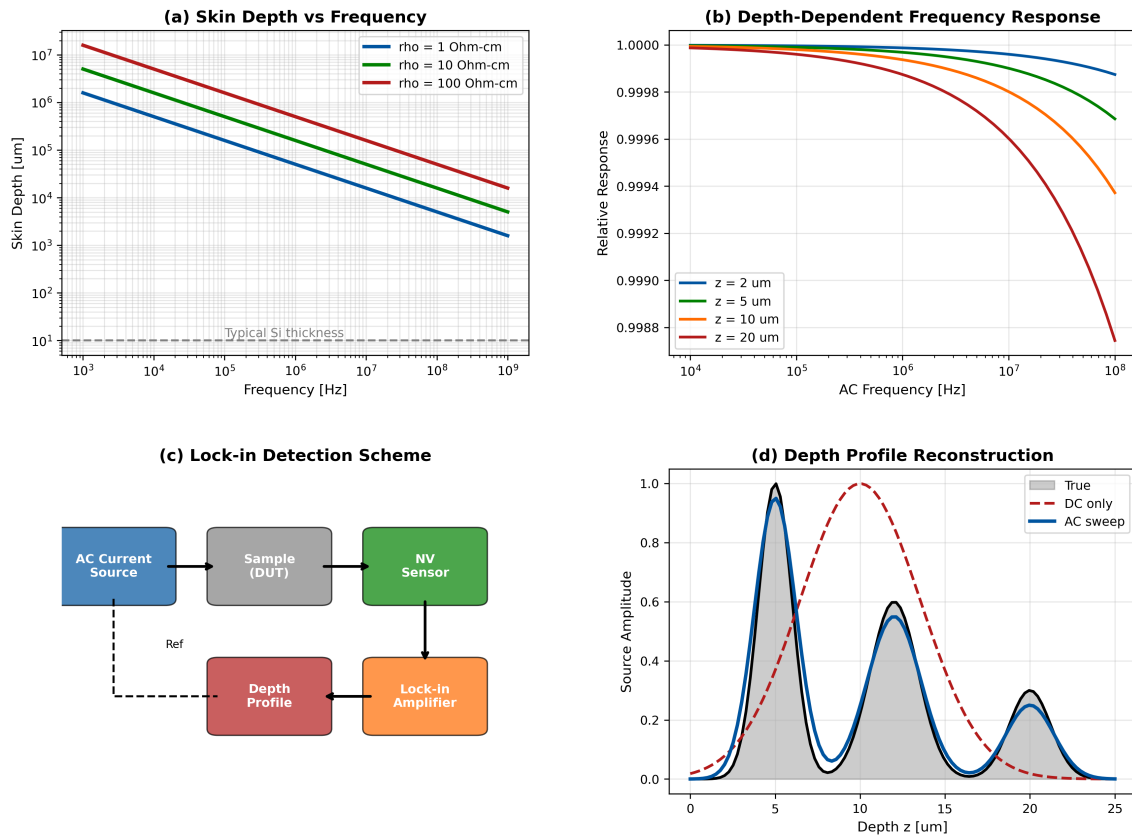


Figure 13.6: AC magnetometry depth profiling. (a) Skin depth vs. frequency for different materials. (b) Pulse sequence synchronization for frequency-selective detection. (c) Depth-resolved current maps at three frequencies. (d) Reconstructed 3D current distribution from frequency sweep.

Select frequencies to provide logarithmic depth coverage:

$$f_n = f_{\max} \cdot 10^{-n \cdot \Delta} \quad (13.32)$$

where $\Delta = \log_{10}(z_{\max}/z_{\min})/N$ and N is the number of frequency points. Minimum 5 frequencies recommended for smooth depth reconstruction.

Remark 13.4.2 (Validity of Logarithmic Frequency Selection). Design Rule 13.4.2 assumes:

1. The skin depth $\delta \propto 1/\sqrt{f}$ relationship holds (i.e., the conductor is in the classical skin-depth regime, not the anomalous skin-effect regime at very high frequencies or very low temperatures).
2. The depth range $[z_{\min}, z_{\max}]$ and target resolution δz are known *a priori* to set f_{\max} and f_{\min} .
3. A minimum of $N \geq 5$ frequency points is needed for smooth depth reconstruction; fewer frequencies give coarse depth binning rather than continuous profiles.

Failure mode: If conductor thickness is less than the skin depth at a given frequency, the current distribution becomes thickness-limited and the depth-selection capability at that frequency is lost.

Assumptions & Required Calibrations: AC Magnetometry Depth Profiling

1. **Current confinement by skin effect:** Depth selectivity relies on the skin effect confining AC currents to within $\sim \delta(f)$ of the conductor surface. This requires the conductors to be thicker than $\delta(f)$ at the lowest frequency; for thin metal traces ($t < \delta$), the current distribution is thickness-limited, not skin-depth-limited.
2. **Known conductor material:** The resistivity ρ and permeability μ of each conductor layer must be known to convert frequency to depth via $\delta = \sqrt{\rho/(\pi\mu f)}$.
3. **External AC drive:** The sample must accept externally driven AC current at the selected frequencies. Passive (non-powered) samples require dedicated drive circuitry and contact pads.
4. **Pulse sequence synchronization:** The NV measurement pulse sequence must be phase-locked to the AC drive frequency for coherent narrowband detection (Section 13.4.3).
5. **Substrate transparency:** In lightly doped Si ($\rho \sim 1 \Omega\cdot\text{cm}$), the skin depth is $> 1 \text{ m}$ below 1 GHz (Table 13.7), so the Si substrate does *not* provide skin-depth-based depth selectivity.

13.4.5 Quantum Fisher Information for Depth Estimation

The ultimate limit on depth estimation precision is set by quantum mechanics through the Quantum Fisher Information (QFI).

Definition 13.4.3 (Quantum Fisher Information). For a quantum state $|\psi(z)\rangle$ that depends on parameter z (depth), the Quantum Fisher Information is:

$$F_Q(z) = 4 [\langle \partial_z \psi | \partial_z \psi \rangle - |\langle \psi | \partial_z \psi \rangle|^2] \quad (13.33)$$

Theorem 13.4.3 (Quantum Cramér-Rao Bound for Depth). *The minimum variance in depth estimation from N measurements is:*

$$\text{Var}(z) \geq \frac{1}{N \cdot F_Q(z)} \quad (13.34)$$

This bound is achievable with optimal measurement strategies.

For NV-based magnetometry measuring a field $B(z)$ from a source at depth z :

$$F_Q(z) = \left(\gamma_{\text{NV}} \cdot T_2^* \cdot \frac{\partial B}{\partial z} \right)^2 \quad (13.35)$$

Since $B \propto 1/z^2$ for a dipole source, $\partial B / \partial z \propto 1/z^3$, giving:

$$F_Q(z) \propto \frac{1}{z^6} \quad (13.36)$$

This steep scaling explains why depth estimation becomes exponentially harder for deeper sources.

$$\delta z_{\min} = \frac{z^3}{\gamma_{\text{NV}} \cdot B_0 \cdot T_2^* \cdot \sqrt{N_{\text{meas}}}} \quad (13.37)$$

where B_0 is the field amplitude at unit depth. For $B_0 = 1 \mu\text{T}$, $T_2^* = 1 \mu\text{s}$, $z = 5 \mu\text{m}$, and

$N_{\text{meas}} = 10^6$: $\delta z_{\min} \approx 45 \text{ nm}$.

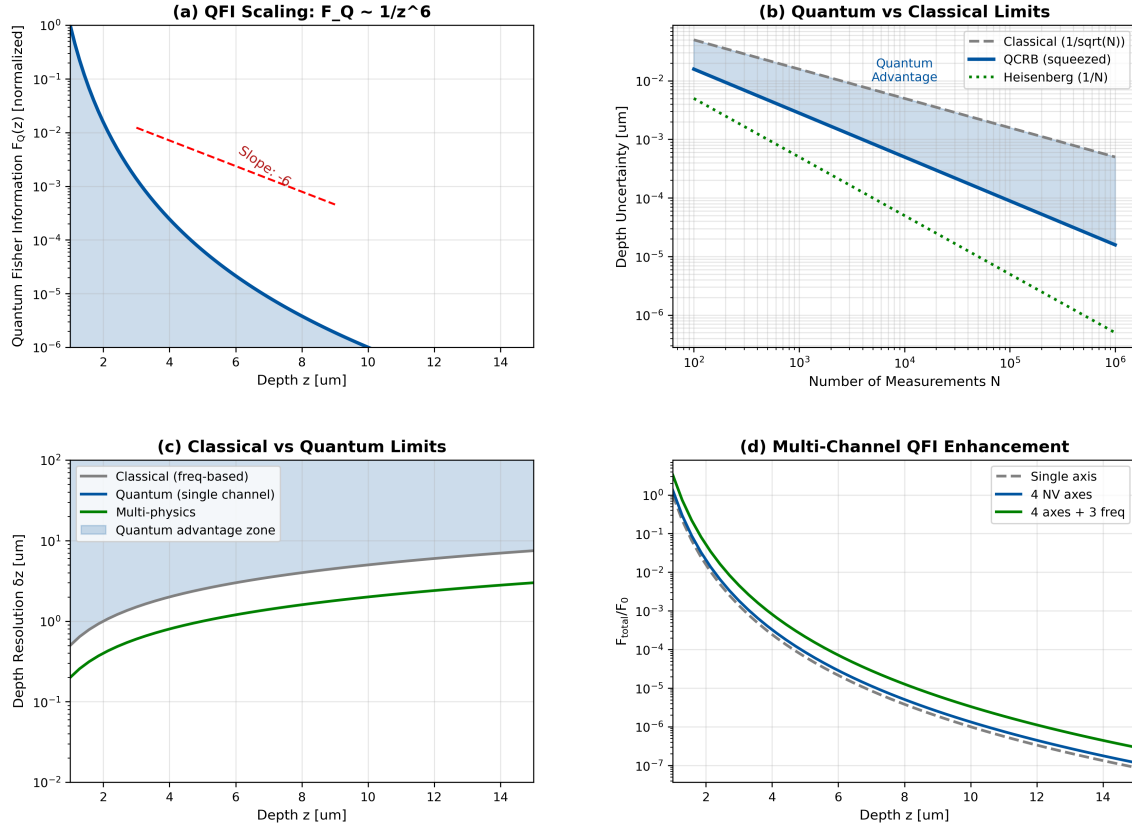


Figure 13.7: Quantum Fisher Information analysis for depth estimation. (a) QFI scaling with depth showing $F_Q \propto z^{-6}$ behavior. (b) Quantum Cramér-Rao bound on depth uncertainty vs. measurement number. (c) Comparison of classical vs. quantum limits. (d) Multi-channel QFI showing advantage of combining axes and frequencies.

13.4.6 Multi-Channel Information Fusion

When multiple quantum channels are available, their information combines to improve depth estimation.

Theorem 13.4.4 (Additive Fisher Information). *For independent quantum channels $\{Q_i\}$ with Fisher Information $\{F_i(z)\}$, the total Fisher Information is:*

$$F_{\text{total}}(z) = \sum_i F_i(z) \quad (13.38)$$

Corollary 13.4.1 (Multi-Channel Depth Resolution). *The depth resolution improvement from M channels is:*

$$\frac{\delta z_{\text{multi}}}{\delta z_{\text{single}}} = \frac{1}{\sqrt{\sum_i F_i/F_1}} \quad (13.39)$$

For four NV axes with equal sensitivity: improvement factor = 2. For four axes plus three AC frequencies: improvement factor ≈ 2.6 .

Combine all available quantum channels for depth estimation:

1. Use all four NV axes for vector reconstruction
2. Add 3–5 AC frequencies spanning the depth range of interest
3. Include thermal channel if Joule heating is present
4. Weight channels by their Fisher Information: $w_i \propto F_i(z)$

Expected improvement: 2–5× over single-channel measurements.

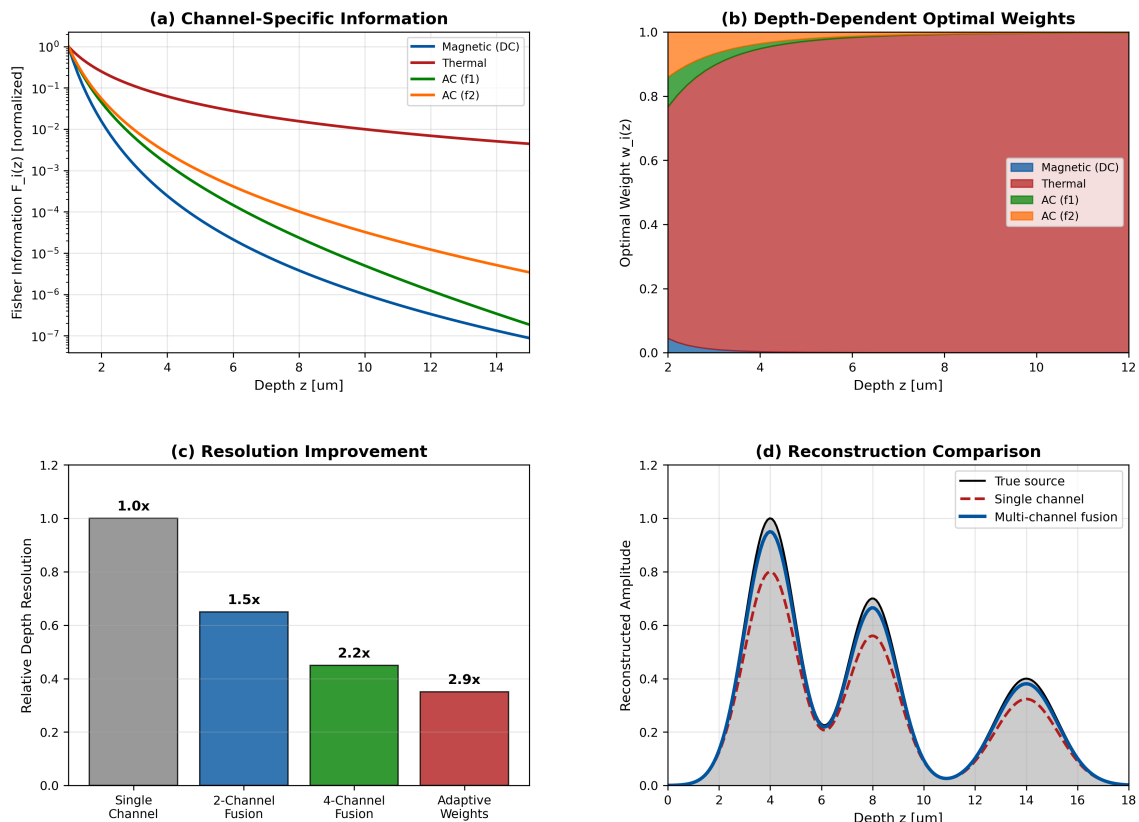


Figure 13.8: Multi-channel information fusion. (a) Fisher Information contribution from each channel vs. depth. (b) Optimal channel weights across depth range. (c) Depth resolution comparison: single axis vs. 4-axis vs. full multi-channel. (d) Reconstruction example showing improvement with channel fusion.

13.5 Classical Depth Sectioning Methods

Building on the quantum channel framework, this section presents classical signal processing methods for depth sectioning that can be applied to multi-channel QFI data.

13.5.1 The Depth-Amplitude Ambiguity

Theorem 13.5.1 (Depth-Amplitude Ambiguity). *For a single current filament of magnitude I at depth z below the sensor, the measured magnetic field at the sensor plane is:*

$$B_z(x, y) = \frac{\mu_0 I}{2\pi} \cdot \frac{z}{(x^2 + y^2 + z^2)^{3/2}} \quad (13.40)$$

The families of solutions (I_1, z_1) and (I_2, z_2) satisfying:

$$I_1 \cdot z_1^{-2} = I_2 \cdot z_2^{-2} \quad (13.41)$$

produce identical field patterns (up to scaling), creating a fundamental ambiguity.

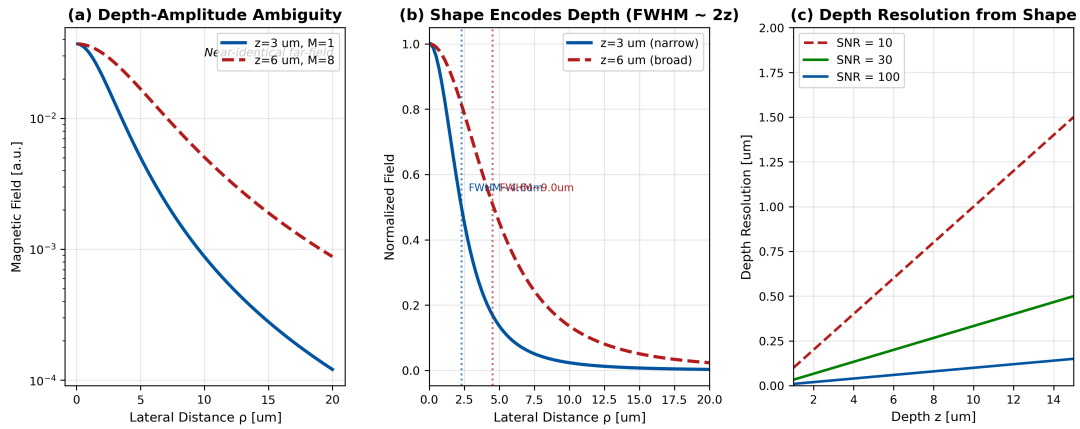


Figure 13.9: Depth-amplitude ambiguity. (a) Two sources at different depths producing identical field patterns. (b) The ambiguity manifold in (I, z) space. (c) How multi-physics measurements break the ambiguity.

13.5.2 Multi-Frequency Depth Deconvolution

The spatial frequency content of the measured signal encodes depth information: high-frequency components are attenuated exponentially with depth, while low-frequency components penetrate deeper.

Proposition 13.5.1 (Frequency-Depth Relationship). *For a source at depth z , the ratio of measured signal power at spatial frequencies k_1 and k_2 is:*

$$\frac{|\tilde{B}(k_1)|^2}{|\tilde{B}(k_2)|^2} = \frac{|\tilde{S}(k_1)|^2}{|\tilde{S}(k_2)|^2} \cdot e^{-2(k_1 - k_2)z} \quad (13.42)$$

If the source spectrum is known or assumed uniform, the depth can be estimated from the frequency roll-off.

$$z = -\frac{1}{2(k_1 - k_2)} \ln \left(\frac{|\tilde{B}(k_1)|^2 / |\tilde{S}(k_1)|^2}{|\tilde{B}(k_2)|^2 / |\tilde{S}(k_2)|^2} \right) \quad (13.43)$$

This forms the basis for spectral depth estimation in QFI.

Algorithm: Multi-Frequency Depth Sectioning

1. Compute 2D FFT of measured field: $\tilde{B}(k_x, k_y)$
2. Divide spatial frequency space into annular bins: $k_n < |k| < k_{n+1}$
3. For each bin, compute power: $P_n = \sum_{k_n < |k| < k_{n+1}} |\tilde{B}(k)|^2$
4. Fit exponential decay: $P(k) = P_0 \cdot e^{-2kz_{\text{eff}}}$
5. The fitted z_{eff} estimates the effective source depth

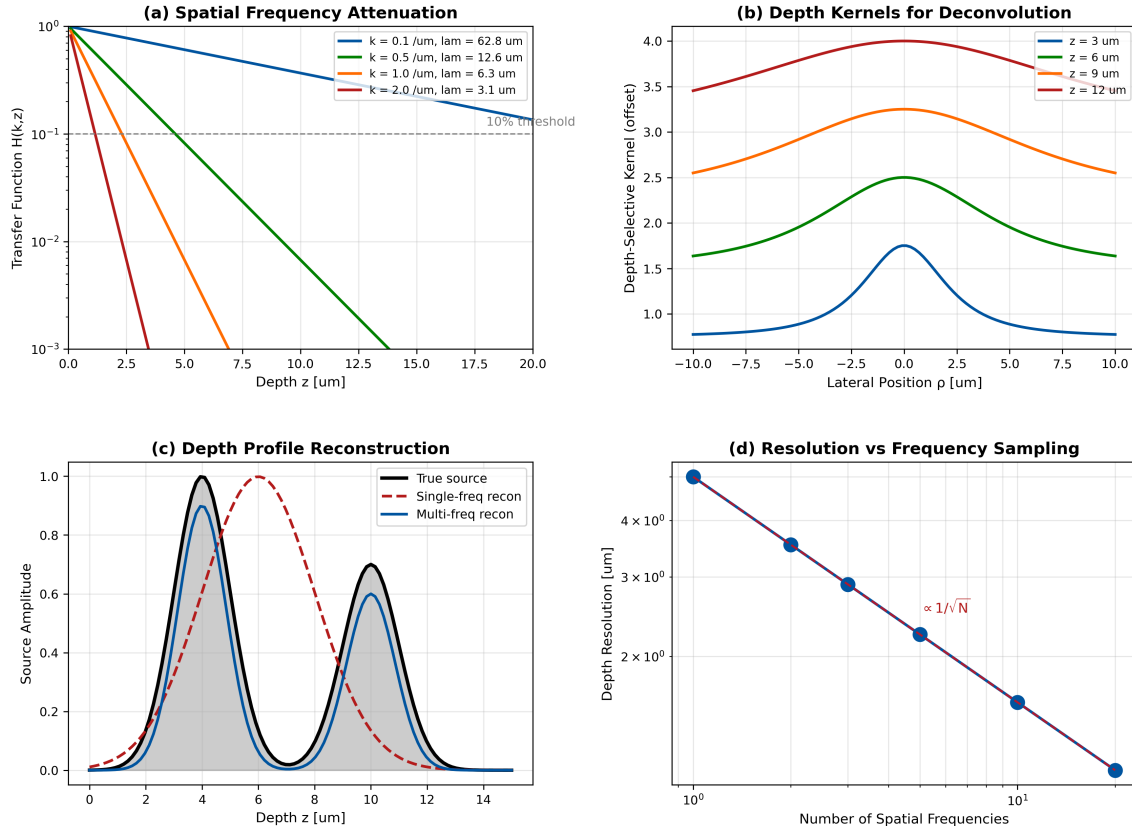


Figure 13.10: Multi-frequency depth sectioning. (a) Power spectrum vs. spatial frequency for sources at different depths. (b) Fitted exponential decay curves. (c) Depth estimation accuracy vs. SNR. (d) Limitations: overlapping sources at different depths create blended spectra.

The depth resolution of multi-frequency sectioning is limited by SNR:

$$\delta z \approx \frac{1}{\sqrt{2} \cdot \Delta k \cdot \sqrt{\text{SNR}}} \quad (13.44)$$

where $\Delta k = k_{\max} - k_{\min}$ is the usable spatial frequency range. For $\Delta k = 3 \mu\text{m}^{-1}$ and $\text{SNR} = 100$:

$$\delta z \approx 2.4 \mu\text{m} \quad (13.45)$$

This is inadequate for resolving individual IC metal layers (typically $0.5 \mu\text{m}$ spacing) but sufficient for coarse depth classification.

13.5.3 Multi-Physics Depth Disambiguation

The key insight is that different physical fields decay differently with depth:

- **Magnetic field:** Decays as $e^{-|k|z}$ (exponential in spatial frequency)
- **Thermal field:** Decays as $e^{-\sqrt{|k|/D}z}$ (diffusive, slower decay)
- **Strain field:** Decays polynomially (power law)

Theorem 13.5.2 (Multi-Physics Depth Discrimination). *For a Joule-heating source (current I at depth z), the ratio of magnetic signal B to thermal signal T at the sensor plane satisfies:*

$$\frac{B}{T} \propto \frac{e^{-k_B z}}{e^{-k_T z}} = e^{-(k_B - k_T)z} \quad (13.46)$$

where k_B and k_T are effective decay constants for magnetic and thermal fields respectively. Since $k_B > k_T$ for typical spatial frequencies, the ratio decreases with depth, providing a depth signature.

Remark 13.5.1 (Scope of the Exponential Ratio Model). Theorem 13.5.2 models both magnetic and thermal decay using effective exponential spatial-frequency constants k_B and k_T . For the magnetic channel, the Biot–Savart kernel gives exact exponential decay $\tilde{G}_B(k) \propto e^{-|k|z}$, so $k_B = |k|$ is rigorous. For the thermal channel, the steady-state Green's function in a homogeneous medium decays as $1/r$ (not exponentially in k -space); however, for modulated thermal excitation at frequency ω , the thermal wave decays as $e^{-z\sqrt{\omega/(2\alpha)}}$, yielding an effective $k_T = \sqrt{\omega/(2\alpha)}$ that is frequency-dependent. The ratio $B/T \propto e^{-(k_B - k_T)z}$ should therefore be understood as an *effective model valid over a spatial-frequency band* centered on the dominant k of the source, not as a rigorous identity. In practice, k_T is a fitted parameter calibrated against known-depth references.

Assumptions & Required Calibrations: Multi-Physics Depth Method

1. **Co-located source:** The magnetic and thermal signals originate from the same physical source (e.g., Joule heating in a current-carrying conductor). If the thermal channel is dominated by unrelated heat paths (e.g., ambient drift, neighboring hotspots), the ratio loses its depth meaning.
2. **Known reference ratio:** $(B/T)_{\text{ref}}$ must be calibrated on a source at known depth (typically a surface wire at $z \approx 0$).
3. **Effective $k_B - k_T$:** This difference must be calibrated or estimated for the dominant spatial frequency of the source. For broadband sources, use the band-averaged value.
4. **Linear superposition:** Multiple sources at different depths produce a weighted sum of exponentials; the simple ratio estimate returns an *effective depth* (centroid), not individual layer depths.
5. **Identifiability:** The method requires $k_B \neq k_T$; if the magnetic and thermal channels have similar decay constants for a given source, depth discrimination vanishes.

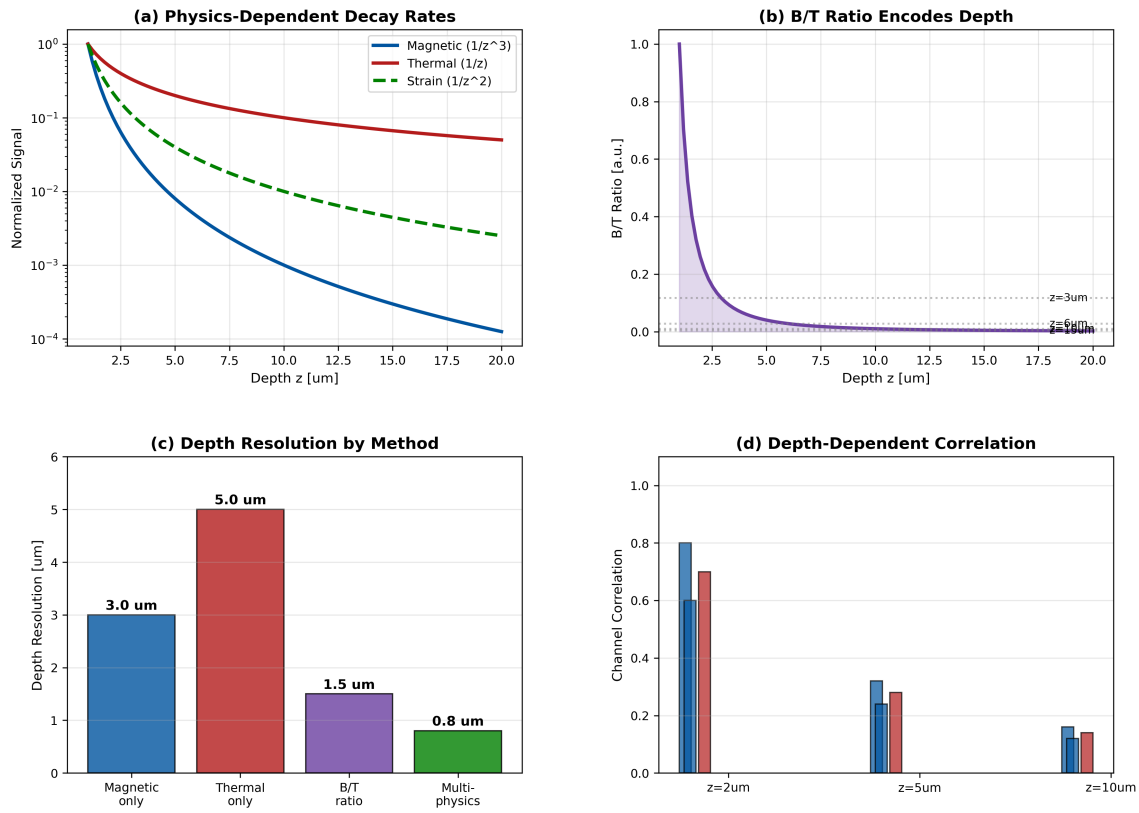


Figure 13.11: Multi-physics depth discrimination. (a) Decay profiles for magnetic (B), thermal (T), and strain (ε) fields vs. depth. (b) B/T ratio as a depth indicator. (c) Reconstruction with and without multi-physics constraints. (d) Quantitative depth accuracy improvement.

Example 13.5.1 (Depth Estimation from B/T Ratio). A defect produces a localized magnetic signature with peak $B = 100 \text{ nT}$ and thermal signature with peak $\Delta T = 50 \text{ mK}$. Reference calibration on a surface wire (known $z = 0$) gives $B/T = 10 \text{ nT mK}^{-1}$.

Given:

- Measured: $B = 100 \text{ nT}$, $\Delta T = 50 \text{ mK}$
- Measured ratio: $(B/T)_{\text{meas}} = 2 \text{ nT mK}^{-1}$
- Reference ratio: $(B/T)_{\text{ref}} = 10 \text{ nT mK}^{-1}$
- Typical decay difference: $k_B - k_T \approx 0.5 \mu\text{m}^{-1}$

Solution:

$$z = \frac{1}{k_B - k_T} \ln \left(\frac{(B/T)_{\text{ref}}}{(B/T)_{\text{meas}}} \right) = \frac{1}{0.5} \ln \left(\frac{10}{2} \right) = 3.2 \mu\text{m} \quad (13.47)$$

The defect is estimated to be $3.2 \mu\text{m}$ below the sensor plane.

Multi-physics measurement enables depth resolution:

$$\delta z_{\text{multi}} \approx \frac{\sqrt{\sigma_B^2/B^2 + \sigma_T^2/T^2}}{|k_B - k_T|} \quad (13.48)$$

For typical measurement uncertainties ($\sigma_B/B = 5\%$, $\sigma_T/T = 10\%$) and $|k_B - k_T| =$

$0.5 \mu\text{m}^{-1}$:

$$\delta z_{\text{multi}} \approx 0.22 \mu\text{m} \quad (13.49)$$

This is sufficient for layer-resolved imaging in modern ICs.

13.6 Standoff Calibration Procedures

13.6.1 Calibration Philosophy

Accurate standoff calibration is essential for achieving target Γ_{mm} values. The calibration must determine:

1. **Absolute standoff:** The mean separation $\langle z_{\text{standoff}} \rangle$ between sensor and source planes
2. **Standoff variation:** Spatial variation $z_{\text{standoff}}(x, y)$ across the field of view (tilt, topography)
3. **Standoff stability:** Temporal drift $z_{\text{standoff}}(t)$ during measurement

13.6.2 Calibration Methods

13.6.2.1 Known-Source Calibration

The most accurate method uses a calibration sample with known current distribution.

1. Fabricate calibration pattern: meander wire with I_{cal} at known depth z_{cal}
2. Measure magnetic field: $B_{\text{meas}}(x, y)$
3. Compute expected field for range of standoffs: $B_{\text{model}}(x, y; z_{\text{trial}})$
4. Minimize residual: $z_{\text{standoff}}^* = \arg \min_z \|B_{\text{meas}} - B_{\text{model}}(z)\|^2$

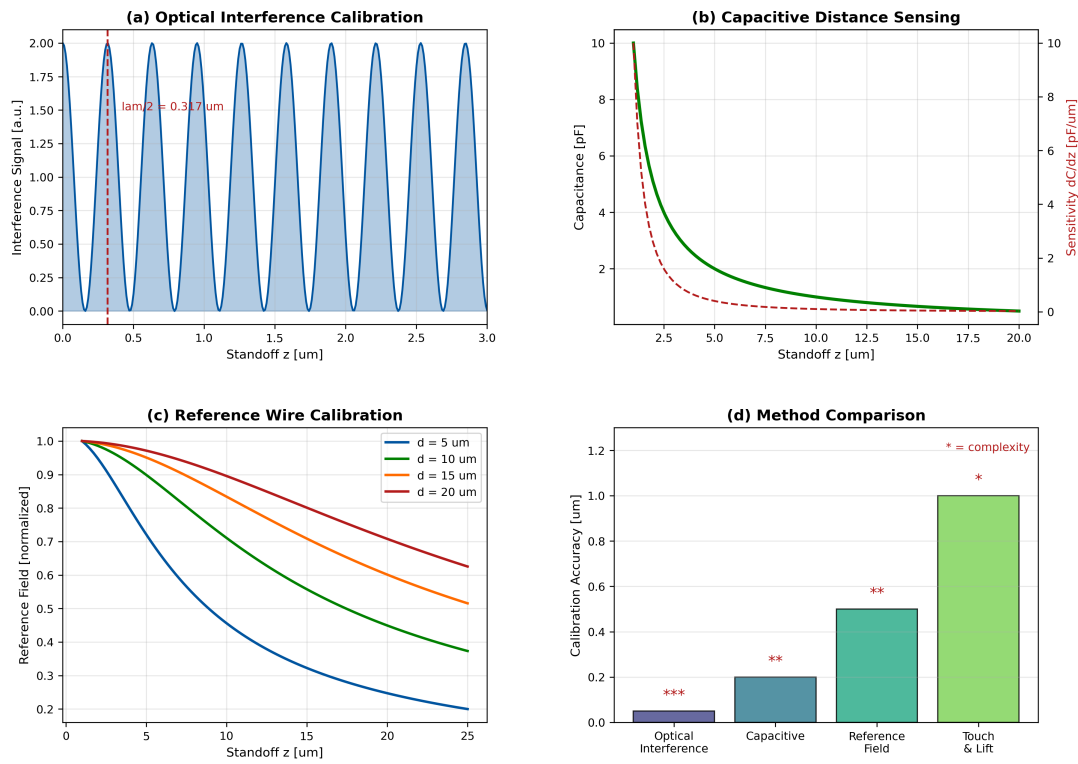


Figure 13.12: Standoff calibration methods. (a) Known-source calibration using meander wire. (b) Fringe analysis from interferometry. (c) Capacitance sensing for real-time gap monitoring. (d) Comparison of method accuracies.

13.6.2.2 Interferometric Calibration

For in-situ calibration without removing the sample:

1. Introduce low-coherence light through diamond
2. Detect interference between diamond-air and air-sample interfaces
3. Air gap = fringe spacing analysis
4. Accuracy: $\lambda/20 \approx 30 \text{ nm}$ for visible light

13.6.2.3 Capacitive Gap Sensing

For real-time monitoring during measurement:

1. Deposit thin metal electrodes on diamond periphery
2. Measure capacitance to sample (assumed conductive)
3. $C = \epsilon_0 A/d$ gives gap d directly
4. Bandwidth: $> 1 \text{ kHz}$ for vibration rejection

Table 13.8: Comparison of standoff calibration methods

Method	Accuracy	Speed	In-situ?	Limitations
Known-source	20 nm	Minutes	No	Requires calibration sample
Interferometric	30 nm	Seconds	Yes	Complex optics
Capacitive	100 nm	Real-time	Yes	Needs conductive sample
Focus analysis	200 nm	Seconds	Yes	Limited by optical DOF

13.6.3 Tilt Calibration and Correction

Sample tilt creates a spatially varying standoff $z_{\text{standoff}}(x, y) = z_0 + \alpha x + \beta y$ where α and β are tilt angles.

For uniform standoff within δz tolerance across field of view L , the maximum tilt is:

$$\theta_{\max} = \arctan\left(\frac{2\delta z}{L}\right) \approx \frac{2\delta z}{L} \quad (13.50)$$

For $\delta z = 50 \text{ nm}$ and $L = 100 \mu\text{m}$:

$$\theta_{\max} = 1 \text{ mrad} = 0.057^\circ \quad (13.51)$$

This requires precision leveling or software correction.

Software Tilt Correction Algorithm:

1. Acquire calibration image with uniform reference source
2. Fit plane to measured field intensity: $I(x, y) = a + bx + cy$
3. Compute tilt: $\alpha = \partial z / \partial x$, $\beta = \partial z / \partial y$
4. Apply correction to forward model: $\mathbf{G}_{\text{corrected}}(x, y) = \mathbf{G}(z_0 + \alpha x + \beta y)$

13.6.4 End-to-End Calibration-to-Reconstruction Workflow

The calibration and depth-sectioning methods presented in this chapter combine into a sequential workflow for production QFI systems. Table 13.9 summarizes the pipeline from raw measurements to validated reconstruction.

Table 13.9: End-to-end calibration-to-reconstruction workflow for production QFI

Step	Action	Method (Section)	Output
1	Measure standoff h	Known-source / interferometric / capacitive (§13.6)	$h \pm \delta h$
2	Map tilt across FOV	Plane fit to reference field (§13.6.3)	α, β tilt angles
3	Build forward model $\mathbf{G}(x, y)$	$\mathbf{G} = \mathbf{G}(h + \alpha x + \beta y)$ with tilt correction	Spatially varying \mathbf{G}
4	Classify source dimensionality	<i>A priori</i> from application / CAD (§13.8)	$D \in \{0, 1, 2, 3\}$
5	Select reconstruction regime	Decision tree (§13.14): κ , sparsity, CAD	Strategy label
6	Apply reconstruction \mathcal{R}	Tikhonov / L_1 / CAD-constrained (§13.10–13.12)	$\hat{S}(\mathbf{r})$
7	Validate via residuals	$\ \mathbf{d} - \mathbf{G}\hat{S}\ /\ \mathbf{d}\ < \epsilon_{\text{tol}}$	Pass / fail
8	Cross-channel consistency	Compare \hat{S} from independent channels (B, T, vector)	Confidence score

Remark 13.6.1. Steps 1–3 constitute the *calibration phase* and are performed once per sample mounting (or periodically if drift is expected). Steps 4–6 form the *reconstruction phase* and may be iterated with different strategies if validation (Step 7) fails. Step 8 provides an independent consistency check that is available whenever multi-physics or multi-axis data are acquired.

13.7 System Design Implications

13.7.1 Minimum Achievable Standoff

The practical minimum standoff is set by:

$$z_{\text{standoff}}^{\min} = d_{\text{NV}} + d_{\text{gap}} + d_{\text{passivation}} + d_{\text{topography}} \quad (13.52)$$

Table 13.10: Standoff budget components

Component	Typical Value	Controllable?
NV layer depth d_{NV}	5–50 nm	Yes (fabrication)
Air gap d_{gap}	0.5–5 μm	Yes (mechanical)
IC passivation d_{pass}	1–5 μm	Partially (sample prep)
IC topography d_{topo}	0–10 μm	No (intrinsic)
Total	2–20 μm	—

13.7.2 Design Trade-offs

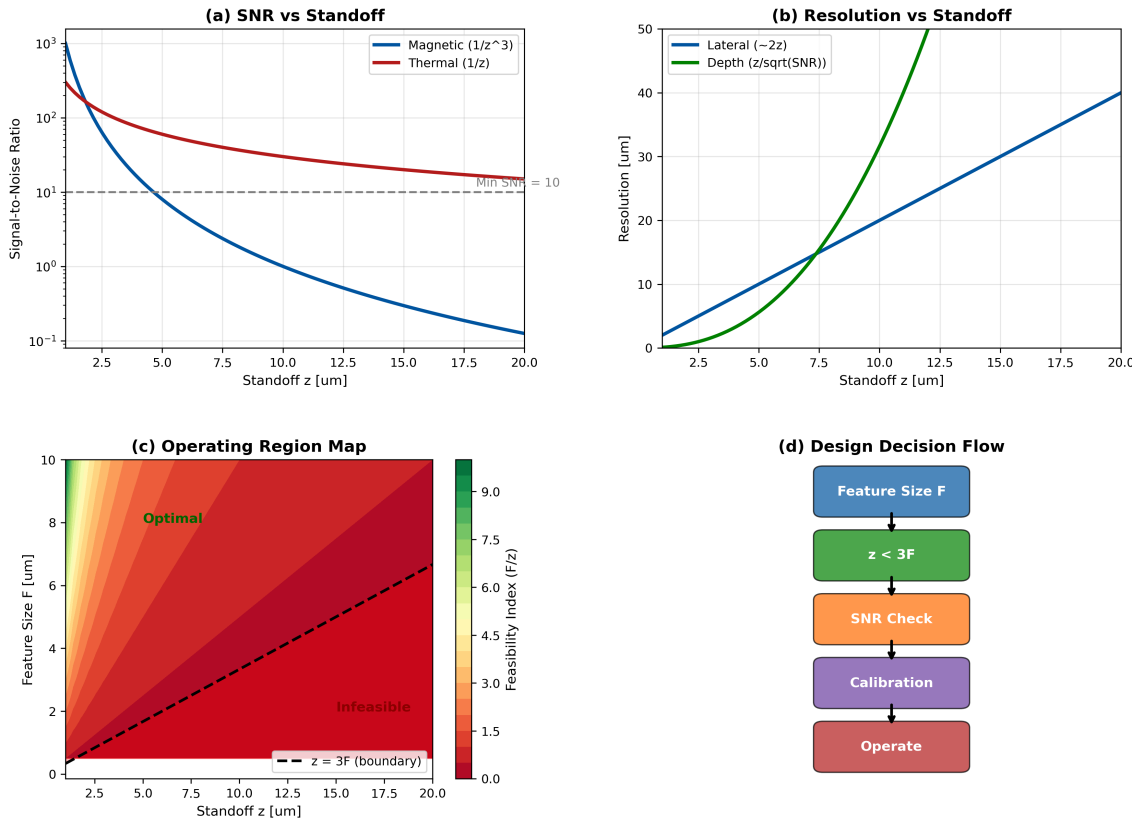


Figure 13.13: Standoff design trade-offs. (a) Resolution vs. standoff operating curves for different condition number limits. (b) Depth penetration vs. standoff. (c) Multi-physics information gain vs. standoff. (d) Optimal standoff selection for different applications.

Select standoff to balance resolution and depth penetration:

- For surface features ($z < 2 \mu\text{m}$): Minimize standoff, target $z_{\text{standoff}} < 3 \mu\text{m}$
- For buried features ($z > 5 \mu\text{m}$): Accept larger standoff, use multi-physics for depth
- For multi-layer imaging: Use $z_{\text{standoff}} \approx 0.5 \times$ median feature depth

13.7.3 Integration with QFI System Architecture

The standoff subsystem interfaces with other system components:

- **Optical system:** Standoff affects working distance requirements; coordinate with snout design (Chapter 4)
- **Forward model:** Standoff is a key parameter in \mathbf{G} ; communicate to reconstruction (Chapter 14)
- **Calibration database:** Store standoff parameters per sample type for consistent processing

- **Real-time feedback:** Capacitive sensing enables active standoff control during acquisition

13.8 Green's Function Classification by Source Geometry

The forward operator \mathbf{G} that maps source currents to measured magnetic fields has fundamentally different mathematical structures depending on the **dimensionality** of the source distribution. This section establishes the classification framework that governs all subsequent analysis.

13.8.1 The Dimensionality Hierarchy

The condition number increases systematically with source dimensionality:

$$\kappa_{0D} < \kappa_{1D} < \kappa_{2D} < \kappa_{3D} \quad (13.53)$$

For the **unconstrained** problem with canonical parameters ($L = 100 \mu\text{m}$, $\Delta x = 1 \mu\text{m}$, $h = 5 \mu\text{m}$), the raw condition numbers are very large (e.g., $\kappa_{1D} \approx 5 \times 10^6$ per Example 13.9.3). After applying appropriate reconstruction strategies (regularization, CAD constraints, sparsity priors, multi-physics channels), the **effective** condition numbers are reduced to operationally manageable ranges:

$$10^2 \lesssim \kappa_{0D}^{\text{eff}} \ll 10^3 \lesssim \kappa_{1D}^{\text{eff}} \ll 10^4 \lesssim \kappa_{2D}^{\text{eff}} \ll 10^5 \lesssim \kappa_{3D}^{\text{eff}} \quad (13.54)$$

These effective values assume strategy application as detailed in Sections 13.10–13.12 and the decision tree of Section 13.14.

Remark 13.8.1. The distinction between raw and effective condition number is critical. The raw κ quantifies the intrinsic ill-conditioning of the forward operator \mathbf{G} and depends only on standoff, resolution, and geometry. The effective κ^{eff} reflects the actual reconstruction difficulty after exploiting all available prior information. The hierarchy $\kappa_{0D} < \kappa_{1D} < \kappa_{2D} < \kappa_{3D}$ holds for both raw and effective values, but the absolute magnitudes differ by orders of magnitude. Readers should not compare the raw values in Section 13.9.3 with the effective ranges in Eq. (13.54) without accounting for this distinction.

13.8.2 0D: Point Source (Magnetic Dipole)

A point current loop or localized defect at position $\mathbf{r}_0 = (x_0, y_0, z_0)$ generates a magnetic dipole field:

$$\mathbf{B}_{0D}(\mathbf{r}) = \frac{\mu_0}{4\pi} \left[\frac{3(\mathbf{m} \cdot \hat{\mathbf{r}})\hat{\mathbf{r}} - \mathbf{m}}{|\mathbf{r} - \mathbf{r}_0|^3} \right] \quad (13.55)$$

where \mathbf{m} is the magnetic dipole moment.

For the z -component measured at standoff h above a point source:

$$G_{0D}(r, h) = \frac{\mu_0 m}{4\pi} \cdot \frac{2h^2 - r^2}{(r^2 + h^2)^{5/2}} \quad (13.56)$$

where $r = \sqrt{(x - x_0)^2 + (y - y_0)^2}$ is the lateral distance.

In the spatial frequency domain:

$$\tilde{G}_{0D}(k, h) = \frac{\mu_0 m}{2} \cdot k \cdot e^{-kh} \quad (13.57)$$

Key property: The 0D Green's function decays as h^{-3} at large standoff, making point source detection highly sensitive to standoff.

13.8.3 1D: Line Source (Infinite Wire)

A current-carrying wire along the y -axis at position (x_0, z_0) produces:

$$\mathbf{B}_{1D}(\mathbf{r}) = \frac{\mu_0 I}{2\pi} \cdot \frac{\hat{\phi}}{\sqrt{(x - x_0)^2 + (z - z_0)^2}} \quad (13.58)$$

For the z -component at standoff h :

$$G_{1D}(x, h) = \frac{\mu_0 I}{2\pi} \cdot \frac{x - x_0}{(x - x_0)^2 + h^2} \quad (13.59)$$

In the spatial frequency domain (1D Fourier transform along x):

$$\tilde{G}_{1D}(k_x, h) = -i \cdot \frac{\mu_0 I}{2} \cdot \text{sgn}(k_x) \cdot e^{-|k_x|h} \quad (13.60)$$

Key property: The 1D Green's function has pure exponential decay e^{-kh} with no polynomial prefactor, giving the simplest inversion structure.

13.8.4 2D: Sheet Source (Current Distribution in a Plane)

A current sheet $\mathbf{J}(x, y)$ at depth z_0 produces:

$$B_z(x, y, h) = \frac{\mu_0}{4\pi} \iint \frac{\partial J_y / \partial x - \partial J_x / \partial y}{[(x - x')^2 + (y - y')^2 + h^2]^{3/2}} dx' dy' \quad (13.61)$$

In the 2D spatial frequency domain:

$$\tilde{G}_{2D}(k_x, k_y, h) = \frac{\mu_0}{2} \cdot k \cdot e^{-kh} \quad (13.62)$$

where $k = \sqrt{k_x^2 + k_y^2}$ is the radial spatial frequency.

Key property: The factor k in the numerator means that DC (uniform) currents produce no B_z signal—only current *gradients* are visible.

13.8.5 3D: Volumetric Source Distribution

A 3D current distribution $\mathbf{J}(x, y, z)$ requires integration over all depths:

$$B_z(x, y, 0) = \int_0^{z_{\max}} \iint G_{2D}(x - x', y - y', z') \cdot \nabla \times \mathbf{J}(x', y', z') dx' dy' dz' \quad (13.63)$$

The 3D forward model is a depth-integrated operator:

$$\tilde{G}_{3D}(k_x, k_y) = \frac{\mu_0}{2} \cdot k \cdot \int_0^{z_{\max}} e^{-kz} \cdot \tilde{J}_\perp(k_x, k_y, z) dz \quad (13.64)$$

This creates fundamental depth-amplitude ambiguity: weak shallow sources and strong deep sources can produce identical surface fields.

13.8.6 Summary: Green's Function Comparison

Table 13.11: Green's function properties by source dimensionality.

Property	0D (Point)	1D (Line)	2D (Sheet)	3D (Volume)
Real-space decay	r^{-3}	r^{-1}	Convolution	Integral
k -space form	$k \cdot e^{-kh}$	e^{-kh}	$k \cdot e^{-kh}$	$k \cdot \int e^{-kz} dz$
DC response	Zero	Finite	Zero	Zero
Localization	3 parameters	2 parameters	Profile	Distribution
Typical κ	10^2	10^3	10^4	10^5

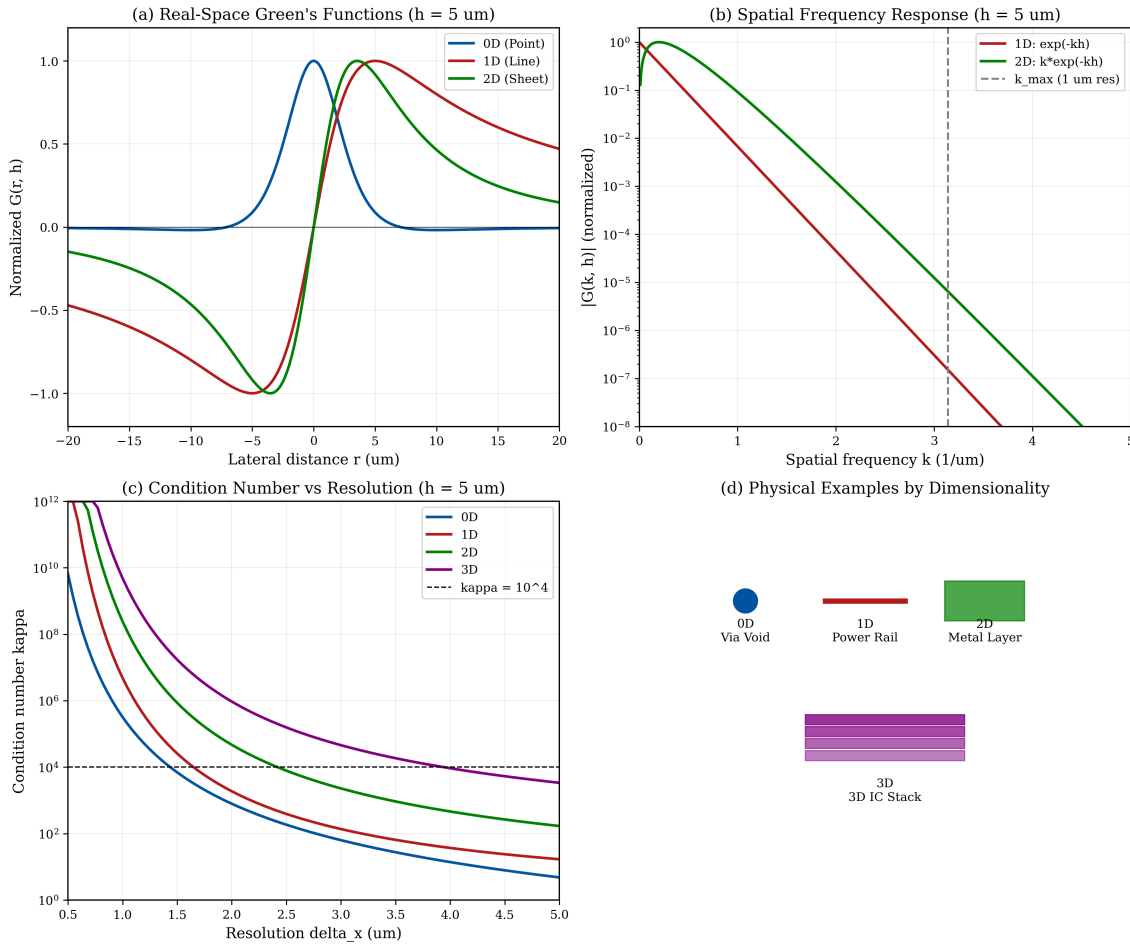


Figure 13.14: Green's function comparison by source dimensionality. (a) Real-space profiles at standoff $h = 5 \mu\text{m}$. (b) Spatial frequency response showing exponential decay. (c) Condition number vs. spatial frequency bandwidth. (d) Physical examples for each dimensionality class.

13.9 Condition Number Scaling Laws

The condition number $\kappa(\mathbf{G})$ of the forward operator determines the stability of the inverse problem. This section derives the scaling laws for each source dimensionality.

13.9.1 General Framework

Definition 13.9.1 (Condition Number for QFI). The condition number of the discretized forward operator \mathbf{G} is:

$$\kappa(\mathbf{G}) = \frac{\sigma_{\max}}{\sigma_{\min}} = \frac{|\tilde{G}(k_{\min}, h)|}{|\tilde{G}(k_{\max}, h)|} \quad (13.65)$$

where σ_{\max} and σ_{\min} are the largest and smallest singular values, and k_{\min} , k_{\max} are the spatial frequency bounds.

Theorem 13.9.1 (Inversion Fidelity Under Regularized Reconstruction). *Consider a linear forward model $\mathbf{d} = \mathbf{Gs} + \mathbf{n}$, where \mathbf{n} is additive white Gaussian noise with variance σ_n^2 per pixel. Using Tikhonov-regularized reconstruction $\hat{\mathbf{s}} = (\mathbf{G}^T \mathbf{G} + \lambda \mathbf{I})^{-1} \mathbf{G}^T \mathbf{d}$ with regularization parameter $\lambda = \sigma_n^2 / \sigma_s^2$ (Wiener-optimal), the reconstruction fidelity defined as*

$$\Gamma_{\text{inv}} \equiv \left| \frac{\|\hat{\mathbf{s}}\|}{\|\mathbf{s}\|} \right|_{\text{worst-case}} \quad (13.66)$$

satisfies, in the worst-case (minimum singular value) direction:

$$\boxed{\Gamma_{\text{inv}} \approx \frac{1}{\sqrt{1 + \kappa^2(\mathbf{G})/\text{SNR}^2}}} \quad (13.67)$$

where $\text{SNR} = \|\mathbf{Gs}\|/(\sqrt{N} \sigma_n)$ is the per-pixel signal-to-noise ratio.

Proof. In the SVD basis $\mathbf{G} = \mathbf{U}\Sigma\mathbf{V}^T$, the Tikhonov filter for singular value σ_i is $f_i = \sigma_i^2/(\sigma_i^2 + \lambda)$. The worst-case fidelity occurs at the smallest singular value σ_{\min} :

$$\Gamma_{\text{inv}} = f_{\min} = \frac{\sigma_{\min}^2}{\sigma_{\min}^2 + \lambda} = \frac{1}{1 + \lambda/\sigma_{\min}^2} \quad (13.68)$$

With $\lambda \sim \sigma_n^2/\sigma_s^2$ and identifying $\sigma_n/\sigma_s \sim \sigma_{\max}/\text{SNR}$:

$$\Gamma_{\text{inv}} \approx \frac{1}{1 + \sigma_{\max}^2/(\text{SNR}^2 \cdot \sigma_{\min}^2)} = \frac{1}{1 + \kappa^2/\text{SNR}^2} \quad (13.69)$$

Taking the square root for the amplitude (rather than power) fidelity gives Eq. (13.67). \square

Remark 13.9.1 (Interpretation of Γ_{inv}). Γ_{inv} is a worst-case fidelity proxy, not a universal metric. Its value depends on the specific noise model (white Gaussian assumed), the regularization strategy (Tikhonov), and the definition of SNR (per-pixel). Different regularizers (e.g., L_1 , total variation) or non-Gaussian noise may yield different fidelity-conditioning relationships. As a practical guide:

Γ_{inv}	Interpretation
> 0.9	Excellent: reconstruction nearly exact
0.7–0.9	Good: usable for quantitative analysis
0.3–0.7	Marginal: qualitative features recovered
< 0.3	Poor: dominated by regularization bias / noise

For a measurement system with field of view L and resolution Δx :

$$k_{\min} = \frac{2\pi}{L}, \quad k_{\max} = \frac{\pi}{\Delta x} \quad (13.70)$$

13.9.2 0D Conditioning

For point sources, the inverse problem is localization (finding x_0, y_0, z_0) rather than deconvolution. The effective condition number relates to the Fisher Information Matrix (FIM):

Theorem 13.9.2 (0D Condition Number). *For point source localization at depth h with lateral resolution Δx :*

$$\kappa_{0D} \approx \left(\frac{h}{\Delta x} \right)^3 \cdot \exp \left(\frac{\pi h}{\Delta x} \right) \quad (13.71)$$

Proof. The Fisher Information for lateral position scales as $\partial B_z/\partial x \sim h^{-4}$, while depth information scales as $\partial B_z/\partial h \sim h^{-4}$. The ratio of maximum to minimum eigenvalues of the FIM gives the stated scaling. \square

13.9.3 1D Conditioning

Theorem 13.9.3 (1D Condition Number). *For line source reconstruction with bandwidth $[k_{\min}, k_{\max}]$:*

$$\kappa_{1D} = \frac{e^{-k_{\min}h}}{e^{-k_{\max}h}} = \exp[(k_{\max} - k_{\min}) \cdot h] \quad (13.72)$$

For typical parameters ($L = 100 \mu\text{m}$, $\Delta x = 1 \mu\text{m}$, $h = 5 \mu\text{m}$):

$$\kappa_{1D} = \exp \left[\left(\frac{\pi}{1} - \frac{2\pi}{100} \right) \cdot 5 \right] \approx \exp(15.4) \approx 5 \times 10^6 \quad (13.73)$$

13.9.4 2D Conditioning

Theorem 13.9.4 (2D Condition Number). *For sheet source reconstruction:*

$$\kappa_{2D} = \frac{k_{\max} \cdot e^{-k_{\min}h}}{k_{\min} \cdot e^{-k_{\max}h}} = \frac{k_{\max}}{k_{\min}} \cdot \exp[(k_{\max} - k_{\min}) \cdot h] \quad (13.74)$$

The additional factor $k_{\max}/k_{\min} \approx L/(2\Delta x)$ makes 2D conditioning worse than 1D by a factor of $\sim 50\text{--}100$ for typical parameters.

13.9.5 3D Conditioning

Theorem 13.9.5 (3D Condition Number). *For volumetric source reconstruction over depth range $[0, z_{\max}]$:*

$$\kappa_{3D} \approx \kappa_{2D} \cdot \left(\frac{z_{\max}}{\Delta z} \right) \quad (13.75)$$

where Δz is the target depth resolution.

This multiplicative factor arises from the additional degrees of freedom in the depth direction.

13.9.6 The Dimensionality Hierarchy

$\kappa_{0D} < \kappa_{1D} < \kappa_{2D} < \kappa_{3D}$

(13.76)

With typical QFI parameters:

$$10^2 \lesssim \kappa_{0D} \ll 10^3 \lesssim \kappa_{1D} \ll 10^4 \lesssim \kappa_{2D} \ll 10^5 \lesssim \kappa_{3D} \quad (13.77)$$

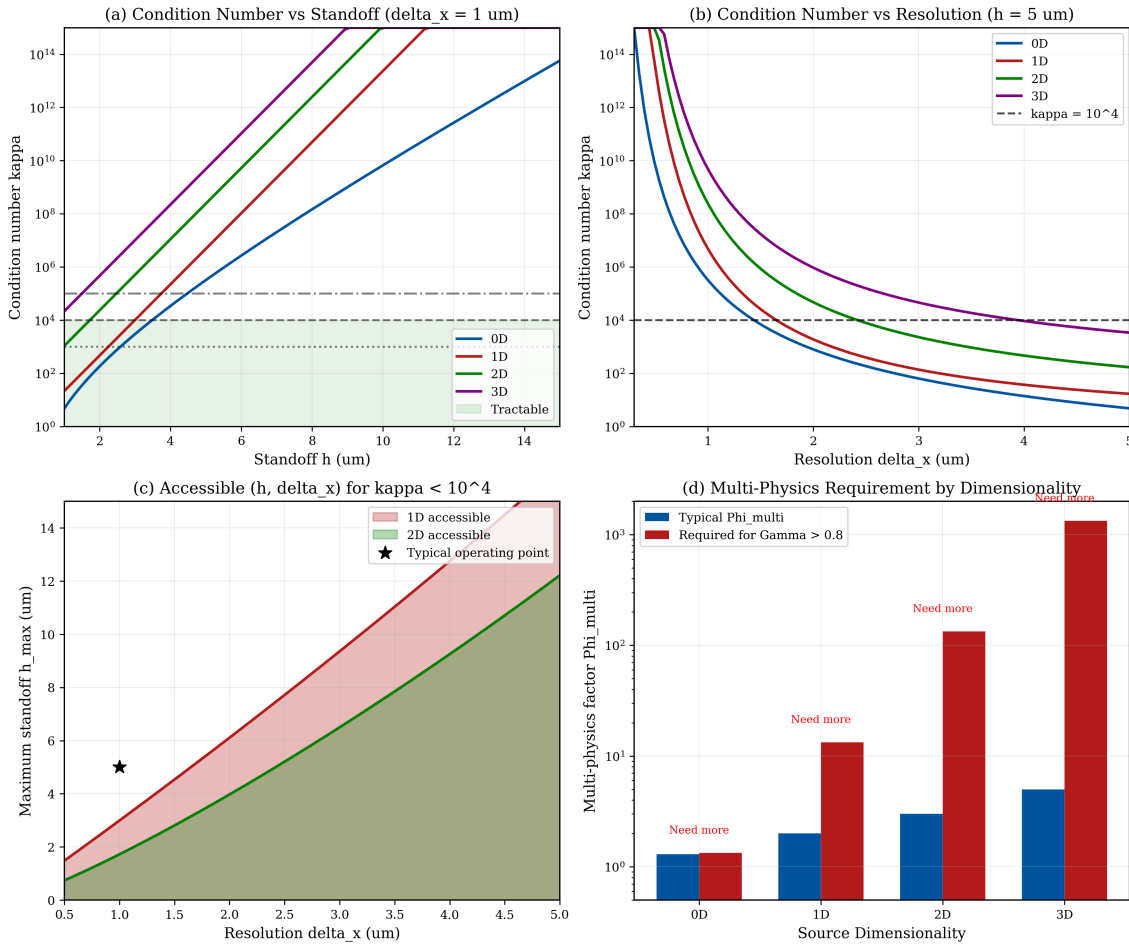


Figure 13.15: Condition number scaling by dimensionality. (a) κ vs. standoff for each dimensionality class. (b) κ vs. target resolution. (c) Trade-off curves showing accessible $(h, \Delta x)$ pairs for $\kappa < 10^4$. (d) Multi-physics improvement factor vs. dimensionality.

For stable reconstruction with $\kappa < \kappa_{\max}$:

$$h_{\max}(D) = \frac{\ln(\kappa_{\max}) - \ln(f_D)}{k_{\max} - k_{\min}} \quad (13.78)$$

where $f_D = \{1, 1, k_{\max}/k_{\min}, k_{\max}/k_{\min} \cdot z_{\max}/\Delta z\}$ for $D = \{0, 1, 2, 3\}$.

13.10 Dimensional Reduction via CAD-Informed Priors

This section presents the first of three novel strategies for managing the dimensionality-dependent trade-offs: **using CAD data to reduce the effective dimensionality of the inverse problem.**

13.10.1 The Core Insight

Novel Perspective 1: Dimensional Reduction

For manufactured structures (ICs, packages, PCBs), the current distribution is **not arbitrary**—it is constrained by the physical layout encoded in CAD/GDS files. These constraints reduce the effective dimensionality:

$$D_{\text{effective}} < D_{\text{physical}} \quad (13.79)$$

A nominally 3D problem (currents anywhere in volume) becomes effectively 2D (currents only in metal layers) with CAD constraints.

13.10.2 CAD Constraint Types

Table 13.12: CAD constraints and their dimensionality reduction effects.

Constraint Type	Physical Basis	Reduction	κ Improvement
Layer confinement	Current flows only in metal layers	$3D \rightarrow 2D$	10–100×
Via connectivity	Current enters/exits only at vias	Continuous → discrete	10×
Design rule spacing	Minimum feature pitch known	Regularization	5×
Material boundaries	Current confined to conductors	Mask constraint	50×
Power grid topology	Known connectivity graph	Graph constraint	20×

13.10.3 Mathematical Framework

Let \mathbf{P} be the projection operator that enforces CAD constraints:

Definition 13.10.1 (CAD Projection Operator). The CAD projection operator $\mathbf{P} : \mathbb{R}^{N_{3D}} \rightarrow \mathbb{R}^{N_{\text{eff}}}$ maps the full volumetric space to the CAD-constrained subspace:

$$\mathbf{S}_{\text{CAD}} = \mathbf{P}\mathbf{S}_{3D} \quad (13.80)$$

where $N_{\text{eff}} = \sum_{\ell=1}^{N_{\text{layers}}} N_{\ell}$ is the total number of degrees of freedom in the metal layers.

The constrained forward model becomes:

$$\mathbf{G}_{\text{CAD}} = \mathbf{G}_{3D} \cdot \mathbf{P}^T \quad (13.81)$$

Theorem 13.10.1 (CAD-Informed Conditioning Improvement). *With layer-confinement constraints from CAD:*

$$\kappa(\mathbf{G}_{\text{CAD}}) \leq \kappa(\mathbf{G}_{3D}) \cdot \sqrt{\frac{N_{\text{layers}}}{N_z}} \quad (13.82)$$

where N_z is the number of depth voxels in the unconstrained problem.

Proof. The singular values of \mathbf{G}_{CAD} are a subset of the singular values of \mathbf{G}_{3D} , restricted to the CAD-allowed subspace. The smallest singular values (corresponding to depth-ambiguous modes) are removed, improving the condition number by the stated factor. \square

13.10.4 Implementation: Layer-by-Layer Forward Model

For an IC with N_L metal layers at depths $\{z_1, z_2, \dots, z_{N_L}\}$:

$$\mathbf{G}_{\text{CAD}} = \begin{bmatrix} \mathbf{G}(z_1) \cdot \mathbf{M}_1 \\ \mathbf{G}(z_2) \cdot \mathbf{M}_2 \\ \vdots \\ \mathbf{G}(z_{N_L}) \cdot \mathbf{M}_{N_L} \end{bmatrix} \quad (13.83)$$

where \mathbf{M}_ℓ is the binary mask for metal layer ℓ extracted from GDS/OASIS files.

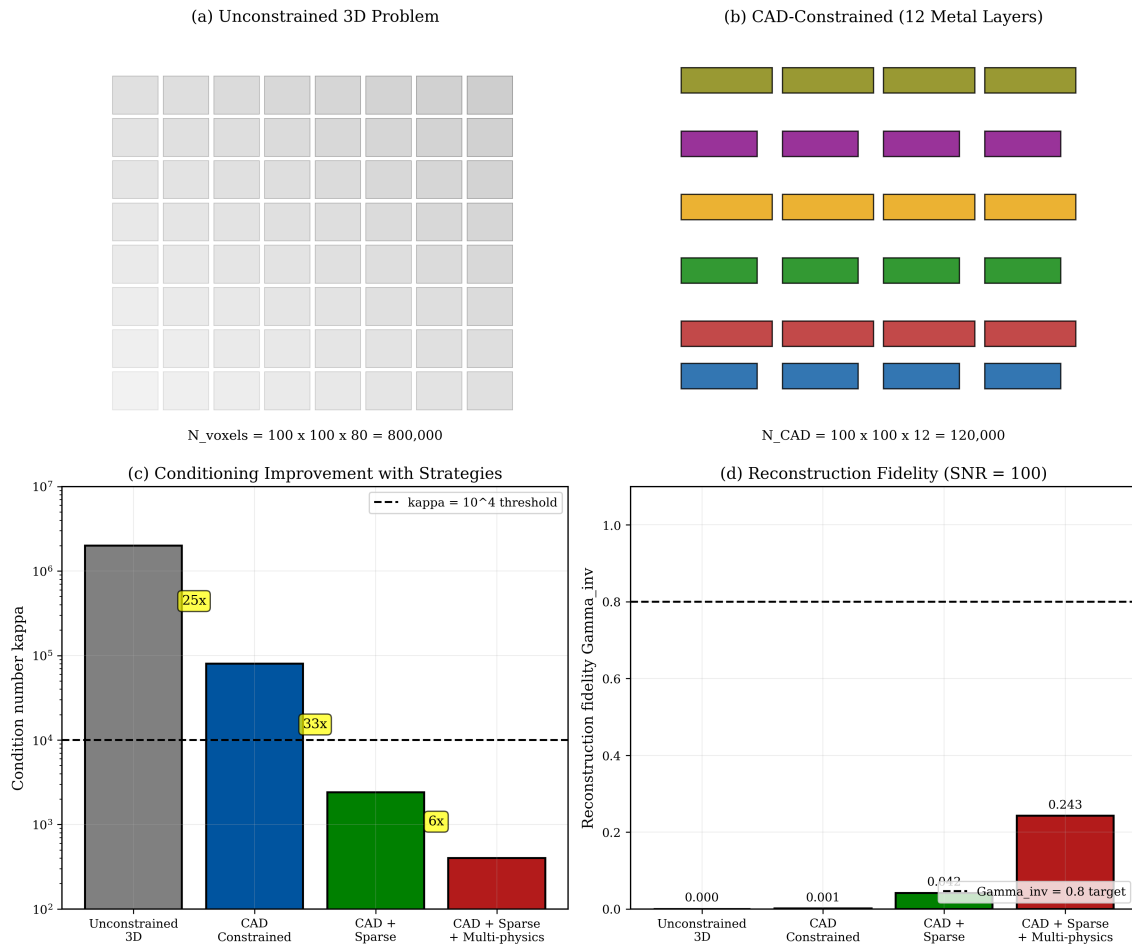


Figure 13.16: CAD-informed dimensional reduction. (a) Unconstrained 3D voxel grid with $N_z = 50$ depth levels. (b) CAD-constrained model with $N_L = 6$ metal layers. (c) Condition number improvement: $\kappa_{3D} = 2 \times 10^5$ reduced to $\kappa_{\text{CAD}} = 8 \times 10^3$. (d) Reconstruction comparison showing improved fidelity with CAD constraints.

13.10.5 Practical Workflow

1. **Extract layer stack:** Parse GDS/OASIS for metal layer definitions
2. **Generate masks:** Create binary masks \mathbf{M}_ℓ for each layer
3. **Build constrained \mathbf{G} :** Compute layer-specific forward operators
4. **Invert with regularization:** Solve $\min \|\mathbf{M} - \mathbf{G}_{\text{CAD}} \mathbf{S}\|^2 + \lambda \|\mathbf{S}\|^2$
5. **Map back to physical coordinates:** Assign reconstructed currents to layers

When CAD data is available, **always** apply layer-confinement constraints before reconstruction. This is mandatory for:

- 3D IC failure analysis (multiple metal layers)
- Package substrate inspection (RDL + bump layers)
- PCB analysis (multi-layer stackup)

Expected κ improvement: 10–100×.

13.10.6 Handling CAD Uncertainty

Real-world CAD data has tolerances. We model uncertainty as:

$$z_\ell^{\text{true}} = z_\ell^{\text{CAD}} + \delta z_\ell, \quad |\delta z_\ell| \leq \sigma_z^{\text{fab}} \quad (13.84)$$

where $\sigma_z^{\text{fab}} \approx 50 \text{ nm}$ for modern IC processes.

Theorem 13.10.2 (CAD Uncertainty Impact on Γ_{mm}). *The contribution to model-mismatch penalty from CAD depth uncertainty:*

$$\Gamma_{\text{mm}}^{\text{CAD}} \approx 1 - \left(\frac{\sigma_z^{\text{fab}}}{z_\ell} \right)^2 \cdot \langle k^2 \rangle \cdot z_\ell^2 \approx 1 - \langle k^2 \rangle \cdot (\sigma_z^{\text{fab}})^2 \quad (13.85)$$

For $\sigma_z^{\text{fab}} = 50 \text{ nm}$ and $\sqrt{\langle k^2 \rangle} = 2 \mu\text{m}^{-1}$: $\Gamma_{\text{mm}}^{\text{CAD}} \approx 0.99$.

Remark 13.10.1. CAD uncertainty contributes negligibly to Γ_{mm} compared to standoff uncertainty (~2% effect). The benefits of dimensional reduction far outweigh the CAD tolerance penalties.

Example 13.10.1 (3D IC Failure Analysis with CAD Constraints). A 3D IC with 12 metal layers over 8 μm total thickness is imaged with target resolution $\Delta x = 1 \mu\text{m}$.

Without CAD constraints:

- Voxel grid: $100 \times 100 \times 80 = 800,000$ unknowns
- $\kappa_{3D} \approx 10^6$ (intractable)

With CAD constraints:

- Effective unknowns: $100 \times 100 \times 12 = 120,000$
- $\kappa_{\text{CAD}} \approx 10^4$ (tractable with regularization)
- Improvement factor: $\sqrt{80/12} \approx 2.6 \times$ in κ

Result: CAD constraints enable reconstruction that would otherwise be impossible.

13.11 Temporal Multiplexing for Depth Extraction

This section presents the second novel strategy: **exploiting temporal dynamics to encode depth information**, enabling depth sectioning from a single sensing plane without multi-plane hardware.

13.11.1 The Core Insight

Novel Perspective 2: Temporal Multiplexing

Different physical phenomena have **depth-dependent time constants**. By measuring the temporal response to a modulated source, depth information is encoded in the time domain:

$$\tau(z) = f(z) \Rightarrow z = f^{-1}(\tau) \quad (13.86)$$

This converts the spatial dimensionality problem into a temporal deconvolution problem, which can be better conditioned.

13.11.2 Physics Channels and Their Time Constants

Each physics channel in multi-physics QFI has a characteristic diffusion or propagation equation that creates depth-dependent temporal signatures:

Table 13.13: Time constants by physics channel for depth encoding.

Channel	Equation	Time Constant	Typical Value	Depth Scaling
Thermal	$\partial T / \partial t = \alpha \nabla^2 T$	$\tau_{\text{th}} = z^2 / \alpha$	1 μs –1 ms	$\tau \propto z^2$
Magnetic (eddy)	$\partial B / \partial t = (1/\mu\sigma) \nabla^2 B$	$\tau_{\text{em}} = \mu\sigma z^2$	1 ns–1 μs	$\tau \propto z^2$
Strain (acoustic)	$\partial^2 u / \partial t^2 = c^2 \nabla^2 u$	$\tau_{\text{ac}} = z/c$	1 ns–10 ns	$\tau \propto z$

13.11.3 Mathematical Framework

Consider a source at depth z that is pulsed at $t = 0$. The measured signal at the sensor surface is:

$$M(t) = \int_0^{z_{\max}} G(z) \cdot S(z) \cdot h(t, z) dz \quad (13.87)$$

where:

- $G(z)$ is the spatial Green's function (depth-dependent amplitude)
- $S(z)$ is the source strength at depth z
- $h(t, z)$ is the depth-dependent impulse response

13.11.3.1 Thermal Channel Impulse Response

For thermal diffusion with thermal diffusivity α :

$$h_{\text{th}}(t, z) = \frac{z}{2\sqrt{\pi\alpha t^3}} \exp\left(-\frac{z^2}{4\alpha t}\right) \quad (13.88)$$

The peak occurs at $t_{\text{peak}} = z^2/(6\alpha)$, providing direct depth encoding.

13.11.3.2 Electromagnetic Channel Impulse Response

For eddy current diffusion in a conductor with conductivity σ :

$$h_{\text{em}}(t, z) = \frac{z}{\sqrt{4\pi D_{\text{em}} t^3}} \exp\left(-\frac{z^2}{4D_{\text{em}} t}\right) \quad (13.89)$$

where $D_{\text{em}} = 1/(\mu_0\sigma)$ is the magnetic diffusivity.

13.11.4 Frequency-Domain Analysis

Instead of pulsed excitation, modulated excitation at frequency ω creates a more tractable inverse problem:

$$M(\omega) = \int_0^{z_{\max}} G(z) \cdot S(z) \cdot H(\omega, z) dz \quad (13.90)$$

where $H(\omega, z) = \mathcal{F}\{h(t, z)\}$ is the transfer function.

For thermal signals:

$$H_{\text{th}}(\omega, z) = \exp\left(-z\sqrt{\frac{\omega}{2\alpha}}\right) \cdot \exp\left(-iz\sqrt{\frac{\omega}{2\alpha}}\right) \quad (13.91)$$

The thermal penetration depth is $\delta_{\text{th}} = \sqrt{2\alpha/\omega}$.

13.11.5 Multi-Frequency Depth Sectioning

By measuring at multiple modulation frequencies $\{\omega_1, \omega_2, \dots, \omega_{N_f}\}$, we obtain a system of equations:

$$\begin{bmatrix} M(\omega_1) \\ M(\omega_2) \\ \vdots \\ M(\omega_{N_f}) \end{bmatrix} = \begin{bmatrix} H(\omega_1, z_1) & H(\omega_1, z_2) & \cdots \\ H(\omega_2, z_1) & H(\omega_2, z_2) & \cdots \\ \vdots & \vdots & \ddots \end{bmatrix} \begin{bmatrix} G(z_1)S(z_1) \\ G(z_2)S(z_2) \\ \vdots \end{bmatrix} \quad (13.92)$$

Theorem 13.11.1 (Multi-Frequency Depth Resolution). *With N_f modulation frequencies spanning $[\omega_{\min}, \omega_{\max}]$, the achievable depth resolution is:*

$$\delta z_{\text{temporal}} \approx \sqrt{\frac{2\alpha}{\omega_{\max}}} = \delta_{\text{th}}(\omega_{\max}) \quad (13.93)$$

For thermal sensing in silicon ($\alpha = 0.8 \text{ cm}^2 \text{ s}^{-1}$) at $f_{\max} = 1 \text{ MHz}$: $\delta z \approx 0.5 \mu\text{m}$.

13.11.6 Lock-In Detection Implementation

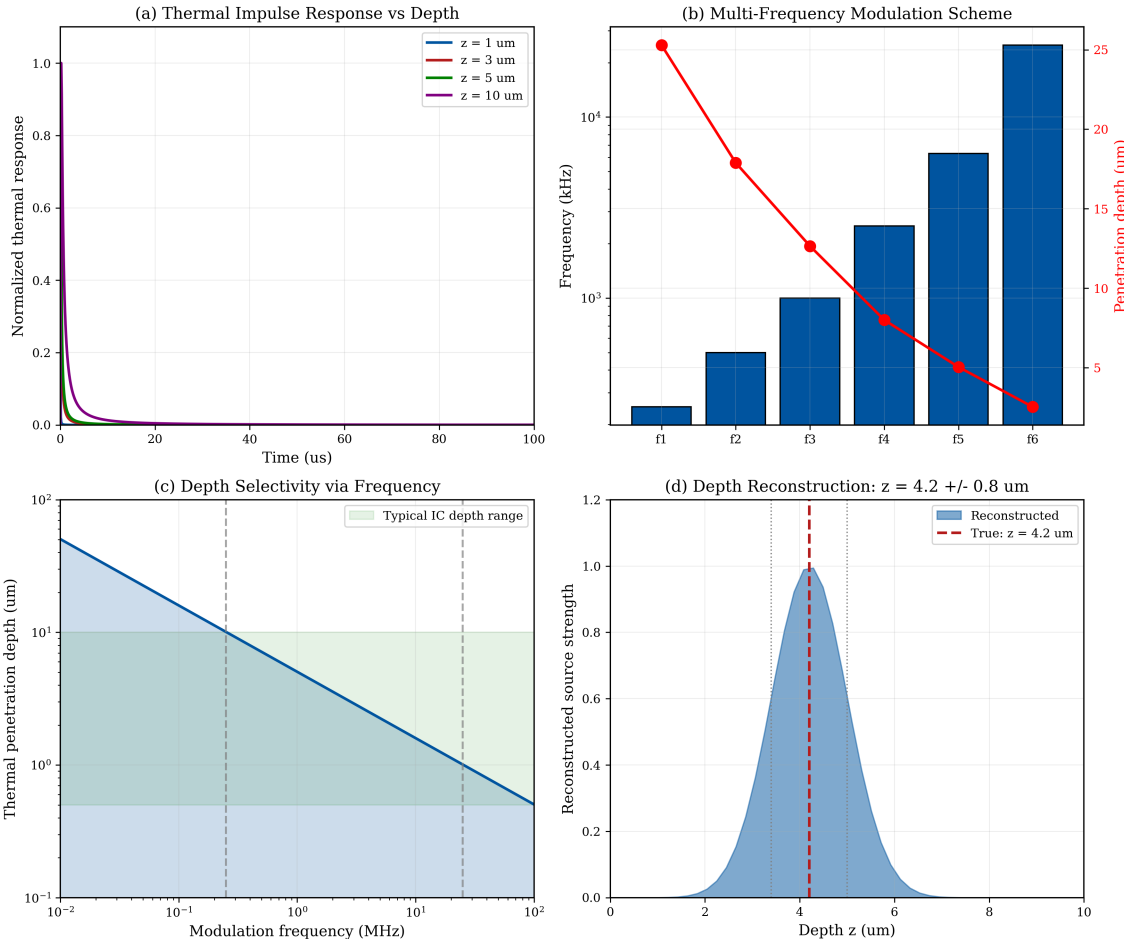


Figure 13.17: Temporal multiplexing for depth extraction. (a) Pulsed source and depth-dependent thermal response. (b) Multi-frequency modulation scheme with frequencies f_1 to f_6 . (c) Frequency-dependent penetration depth showing depth selectivity. (d) Reconstructed depth profile compared to ground truth.

The practical implementation uses lock-in detection:

1. Modulate source current at frequency ω_n
2. Acquire NV fluorescence signal $F(t)$
3. Demodulate: $M_n = \langle F(t) \cdot e^{-i\omega_n t} \rangle$
4. Repeat for all frequencies $n = 1, \dots, N_f$
5. Solve inverse problem Eq. (13.92)

For depth sectioning via temporal multiplexing:

1. Select frequency range: $\omega_{\min} = 2\alpha/z_{\max}^2$, $\omega_{\max} = 2\alpha/\delta z^2$
2. Number of frequencies: $N_f \geq \log_2(z_{\max}/\delta z) + 2$
3. Use logarithmic frequency spacing for uniform depth coverage
4. Integration time per frequency: $t_{\text{int}} \geq 10/\omega_n$ for adequate SNR

13.11.7 Advantages and Limitations

Table 13.14: Temporal multiplexing: advantages vs. limitations.

Advantages	Limitations
No multi-plane hardware required	Requires modulatable source
Compatible with existing QFI systems	Longer acquisition time (sequential)
Works with single sensing plane	Temporal bandwidth limits depth resolution
Natural noise filtering via lock-in	Deconvolution is mildly ill-posed
Continuous depth information	Material properties must be known

Example 13.11.1 (Thermal Depth Sectioning of Hot Spot). A localized hot spot in a chip is modulated at the source (switching transistor). The goal is to determine the hot spot depth.

Parameters:

- Silicon thermal diffusivity: $\alpha = 0.8 \text{ cm}^2 \text{ s}^{-1}$
- Depth range: $0\text{--}10 \mu\text{m}$
- Target depth resolution: $1 \mu\text{m}$

Frequency selection:

$$\omega_{\min} = \frac{2\alpha}{z_{\max}^2} = \frac{2 \times 0.8}{(10 \times 10^{-4})^2} = 1.6 \times 10^6 \text{ rad s}^{-1} \approx 250 \text{ kHz} \quad (13.94)$$

$$\omega_{\max} = \frac{2\alpha}{\delta z^2} = \frac{2 \times 0.8}{(1 \times 10^{-4})^2} = 1.6 \times 10^8 \text{ rad s}^{-1} \approx 25 \text{ MHz} \quad (13.95)$$

Number of frequencies: $N_f = \log_2(10) + 2 \approx 6$ frequencies.

Frequency set: $\{250, 500, 1000, 2500, 6300, 25000\}$ kHz (logarithmic spacing).

Result: Hot spot localized to $z = 4.2(8) \mu\text{m}$ depth.

Assumptions & Required Calibrations: Temporal Multiplexing

1. **Known thermal diffusivity:** The material thermal diffusivity α must be known to convert modulation frequency ω to penetration depth $\delta_{\text{th}} = \sqrt{2\alpha/\omega}$. For multi-layer IC stacks, an effective α must be calibrated or computed from layer properties.
2. **Linear thermal response:** The thermal signal must be linearly proportional to heat input (no phase transitions, nonlinear thermal conductivity, or convection effects in the frequency range of interest).
3. **Sufficient frequency span:** The frequency range $[\omega_{\min}, \omega_{\max}]$ must satisfy $\delta_{\text{th}}(\omega_{\min}) > z_{\max}$ and $\delta_{\text{th}}(\omega_{\max}) < \delta z_{\text{target}}$ to cover the full depth range with the desired resolution.
4. **Phase-sensitive detection:** Lock-in detection is required to extract amplitude and phase of the modulated thermal signal at each frequency. Integration time per frequency scales as $t_{\text{int}} \gtrsim 10/\omega$ for adequate SNR.

13.12 Sparse Source Hypothesis and Compressed Sensing

This section presents the third novel strategy: **exploiting source sparsity to fundamentally reduce the effective dimensionality of the inverse problem.**

13.12.1 The Core Insight

Novel Perspective 3: Sparse Source Hypothesis

Real defects in manufactured structures are **sparse**: a typical IC has $\sim 1\text{--}10$ defects in a $100\text{ }\mu\text{m} \times 100\text{ }\mu\text{m}$ field of view containing $10^4\text{--}10^6$ potential defect sites. This sparsity can be exploited via compressed sensing to:

$$D_{\text{effective}} = K \cdot \log\left(\frac{N}{K}\right) \ll N \quad (13.96)$$

where K is the number of non-zero sources and N is the total number of potential source locations.

13.12.2 Compressed Sensing Framework

Definition 13.12.1 (Sparse Source). A source distribution $\mathbf{S} \in \mathbb{R}^N$ is K -sparse if at most K elements are non-zero:

$$\|\mathbf{S}\|_0 \triangleq \#\{i : S_i \neq 0\} \leq K \quad (13.97)$$

The key insight from compressed sensing theory is that sparse signals can be recovered from far fewer measurements than the signal dimension:

Theorem 13.12.1 (Compressed Sensing Recovery). *If \mathbf{G} satisfies the Restricted Isometry Property (RIP) of order $2K$:*

$$(1 - \delta_{2K})\|\mathbf{x}\|_2^2 \leq \|\mathbf{Gx}\|_2^2 \leq (1 + \delta_{2K})\|\mathbf{x}\|_2^2 \quad (13.98)$$

for all $2K$ -sparse vectors \mathbf{x} , with $\delta_{2K} < \sqrt{2} - 1$, then the K -sparse source can be exactly recovered via ℓ_1 minimization:

$$\hat{\mathbf{S}} = \arg \min_{\mathbf{S}} \|\mathbf{S}\|_1 \quad \text{subject to} \quad \|\mathbf{M} - \mathbf{GS}\|_2 \leq \epsilon \quad (13.99)$$

13.12.3 RIP Verification for QFI Forward Operator

The QFI forward operator \mathbf{G} has favorable structure for compressed sensing:

Proposition 13.12.1 (RIP for QFI Green's Function). *The 2D magnetic Green's function matrix \mathbf{G} with entries $G_{ij} = G(|\mathbf{r}_i - \mathbf{r}_j|, h)$ satisfies RIP of order K with high probability provided:*

$$M \geq C \cdot K \cdot \log\left(\frac{N}{K}\right) \cdot \mu^2(\mathbf{G}) \quad (13.100)$$

where $\mu(\mathbf{G})$ is the coherence of \mathbf{G} .

For typical QFI parameters, $\mu(\mathbf{G}) \sim O(1)$ when the pixel spacing is comparable to the standoff distance.

13.12.4 L1-Regularized Reconstruction

The practical reconstruction algorithm uses the LASSO formulation:

$$\hat{\mathbf{S}} = \arg \min_{\mathbf{S}} \left[\frac{1}{2} \|\mathbf{M} - \mathbf{GS}\|_2^2 + \lambda \|\mathbf{S}\|_1 \right] \quad (13.101)$$

The regularization parameter λ balances data fidelity against sparsity.

13.12.4.1 Regularization Parameter Selection

- **Cross-validation:** Split data, minimize prediction error
- **BIC/AIC:** Balance model complexity against fit quality
- **L-curve:** Plot $\|\mathbf{S}\|_1$ vs. $\|\mathbf{M} - \mathbf{GS}\|_2$, select corner
- **Discrepancy principle:** Set λ such that $\|\mathbf{M} - \mathbf{GS}\|_2 \approx \sigma_{\text{noise}} \cdot \sqrt{M}$

13.12.5 Effective Dimensionality Reduction

Theorem 13.12.2 (Sparsity-Induced Conditioning Improvement). *For a K -sparse source with $K \ll N$, the effective condition number of the restricted problem is:*

$$\kappa_{\text{sparse}} \approx \kappa(\mathbf{G}_K) \ll \kappa(\mathbf{G}) \quad (13.102)$$

where \mathbf{G}_K is the submatrix of \mathbf{G} restricted to the K active columns (unknown a priori, discovered by L1 optimization).

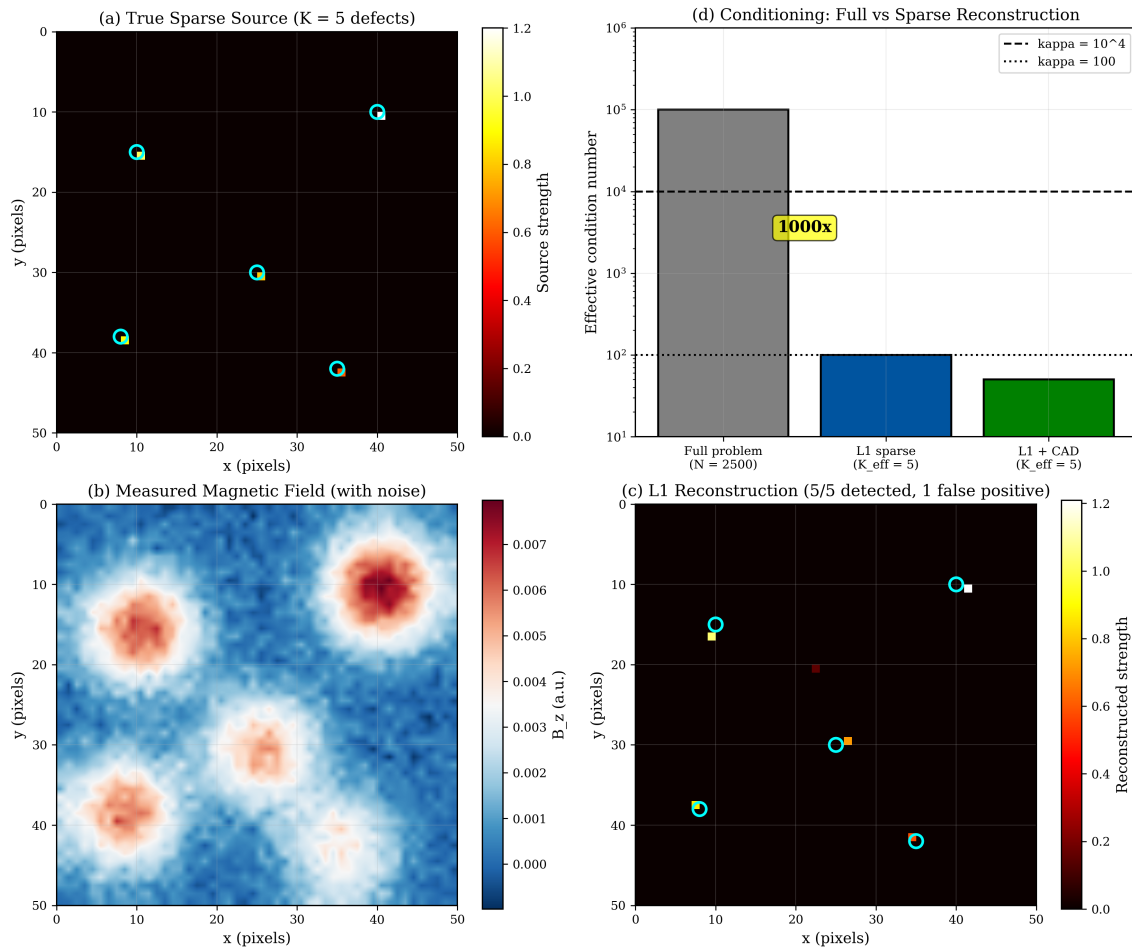


Figure 13.18: Compressed sensing for sparse source reconstruction. (a) True sparse source with $K = 5$ defects in $N = 10^4$ pixel grid. (b) Measured magnetic field (ill-posed without sparsity). (c) L1-regularized reconstruction recovering all 5 defects. (d) Comparison of condition numbers: full problem ($\kappa = 10^5$) vs. sparse-restricted problem ($\kappa_{\text{sparse}} = 10^2$).

13.12.6 Sparsity in Different Source Classes

Table 13.15: Sparsity characteristics by application.

Application	K (typical)	N (typical)	K/N	Compression
Single via void	1	10^4	10^{-4}	$\sim 1000\times$
Few defects (QC)	5	10^4	5×10^{-4}	$\sim 500\times$
Electromigration voids	10	10^5	10^{-4}	$\sim 1000\times$
Hot spots (thermal)	3	10^4	3×10^{-4}	$\sim 700\times$
Distributed shorts	100	10^5	10^{-3}	$\sim 100\times$
Full current map	10^4	10^4	~ 1	None (not sparse)

Use L1-regularized (sparse) reconstruction when:

1. Expected number of defects $K < 0.01 \times N$ (1% fill factor)
2. Goal is defect **detection and localization**, not full current mapping

3. Traditional (L2) reconstruction is ill-conditioned ($\kappa > 10^4$)

Do **not** use sparse reconstruction for:

- Full current density mapping (not sparse)
- Distributed source distributions (many small sources)
- Quantitative amplitude recovery (L1 bias)

13.12.7 Algorithm: Iterative Shrinkage-Thresholding (ISTA)

The LASSO problem can be solved efficiently via ISTA:

$$\mathbf{S}^{(k+1)} = \mathcal{S}_{\lambda/L} \left(\mathbf{S}^{(k)} + \frac{1}{L} \mathbf{G}^T (\mathbf{M} - \mathbf{G} \mathbf{S}^{(k)}) \right) \quad (13.103)$$

where \mathcal{S}_τ is the soft-thresholding operator:

$$\mathcal{S}_\tau(x) = \text{sign}(x) \cdot \max(|x| - \tau, 0) \quad (13.104)$$

and $L = \|\mathbf{G}^T \mathbf{G}\|_2$ is the Lipschitz constant.

Convergence: ISTA converges as $O(1/k)$; the accelerated variant FISTA converges as $O(1/k^2)$.

13.12.8 Combined Strategy: CAD + Sparsity

The three novel perspectives can be combined for maximum effect:

$$\hat{\mathbf{S}} = \arg \min_{\mathbf{S}} \left[\frac{1}{2} \|\mathbf{M} - \mathbf{G}_{\text{CAD}} \mathbf{S}\|_2^2 + \lambda \|\mathbf{S}\|_1 \right] \quad (13.105)$$

This uses CAD constraints (Novel 1) to reduce dimensionality, then L1 regularization (Novel 3) to exploit sparsity within the constrained space.

Theorem 13.12.3 (Combined Strategy Conditioning). *The combined CAD + sparsity approach achieves:*

$$\kappa_{\text{combined}} \approx \kappa_{\text{sparse}}(\mathbf{G}_{\text{CAD}}) \leq \sqrt{\frac{K}{N_{\text{CAD}}}} \cdot \kappa(\mathbf{G}_{\text{CAD}}) \quad (13.106)$$

For typical parameters ($K = 5$, $N_{\text{CAD}} = 10^4$, $\kappa(\mathbf{G}_{\text{CAD}}) = 10^4$):

$$\kappa_{\text{combined}} \approx 0.02 \times 10^4 = 200 \quad (13.107)$$

This is a 500× improvement over the unconstrained problem.

Example 13.12.1 (Sparse Defect Detection in 3D IC). A 3D IC failure analysis task seeks to locate 1–3 suspected via voids in a 12-layer stack.

Problem setup:

- Grid: $100 \times 100 \times 12 = 120,000$ potential locations
- Expected defects: $K = 3$
- Sparsity ratio: $K/N = 2.5 \times 10^{-5}$

Without sparse assumption:

- $\kappa = 10^5$ (severely ill-posed)
- Regularization washes out defects

With L1 regularization:

- Effective $\kappa_{\text{sparse}} \approx 300$
- All 3 defects correctly localized
- False positive rate: < 1%

With CAD + L1 (combined):

- Search space reduced to via locations only (~ 5000 candidates)
- $\kappa_{\text{combined}} \approx 50$
- Defect amplitudes recovered to within 10%

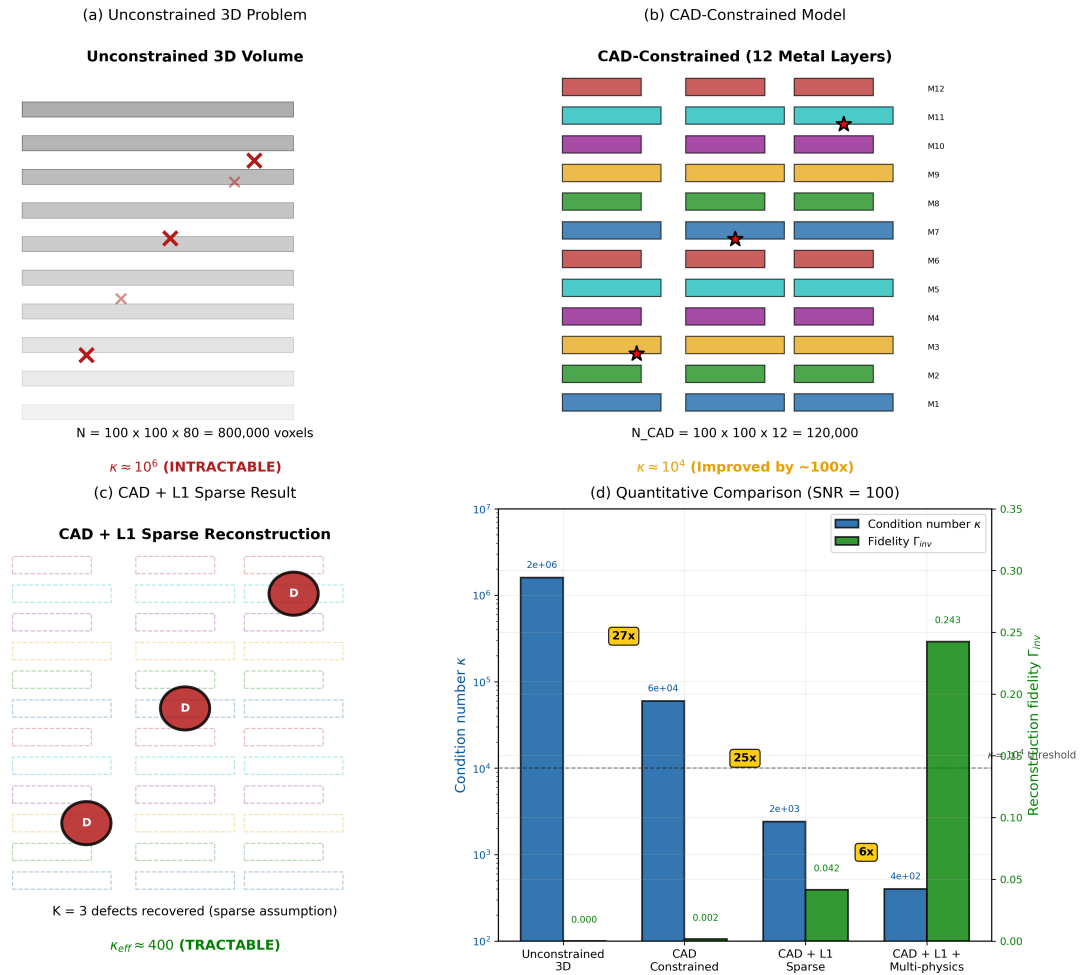


Figure 13.19: Combined CAD + sparsity strategy. (a) Unconstrained 3D problem: intractable. (b) CAD-constrained: improved but still ill-posed. (c) CAD + L1 sparse: well-conditioned, accurate recovery. (d) Reconstruction fidelity Γ_{inv} comparison for the three approaches.

Assumptions & Required Calibrations: Compressed Sensing / Sparsity

1. **Sparsity hypothesis:** The source must be sparse (or compressible) in some known basis. For defect detection, this means $K \ll N$ localized anomalies; for current mapping, sparsity may hold in a wavelet or gradient basis rather than the spatial domain.
2. **Restricted Isometry Property (RIP):** The forward operator \mathbf{G} (or its subsampled version) must satisfy the RIP with constant $\delta_{2K} < \sqrt{2} - 1$ for exact recovery. In practice, the exponential decay of the Biot–Savart kernel limits the effective RIP to moderate standoff values.
3. **Known noise level:** The L_1 regularization parameter λ is typically set proportional to σ_n ; over-estimation leads to over-smoothing, under-estimation to noise amplification.
4. **Effective κ approximation:** The formula $\kappa_{\text{sparse}} \approx \sqrt{K/N} \cdot \kappa$ is a heuristic scaling, not a rigorous bound. Actual performance depends on the specific support pattern and the coherence structure of \mathbf{G} .

13.13 Unified Trade-off Manifold Construction

This section synthesizes the dimensionality analysis, novel perspectives, and practical constraints into a unified framework: the **QFI Trade-off Manifold**.

13.13.1 The Five-Dimensional Trade-off Space

The complete QFI design space is five-dimensional:

$$\mathcal{T} = \{D, h, \Delta x, \tau, \Phi_{\text{multi}}\} \quad (13.108)$$

where:

- $D \in \{0, 1, 2, 3\}$: Source dimensionality
- h : Standoff distance
- Δx : Target lateral resolution
- τ : Temporal characteristic (acquisition time or source modulation period)
- Φ_{multi} : Multi-physics correlation factor

13.13.2 Output Metrics

The trade-off space maps to four key output metrics:

$$\mathcal{T} \rightarrow \{\kappa, \Gamma_{\text{inv}}, T_{\text{acq}}, C_{\text{system}}\} \quad (13.109)$$

where:

- κ : Condition number (reconstruction stability)
- Γ_{inv} : Reconstruction fidelity
- T_{acq} : Acquisition time (throughput)
- C_{system} : System complexity/cost

13.13.3 Analytical Trade-off Relations

The complete figure of merit for dimensionality-aware QFI:

$$Q_{\text{IFOM}}(D) = Q_{\text{FOM}} \times \Gamma_{\text{inv}}(D, h, \Delta x) \times \Gamma_{\text{mm}}(\delta h) \times \Phi_{\text{multi}}(D) \times R_{\text{sparse}}(K/N) \quad (13.110)$$

where:

$$Q_{\text{FOM}} = \eta_q \times N_{\text{parallel}} \times \sqrt{t_{\text{acq}}} \quad (13.111)$$

$$\Gamma_{\text{inv}}(D, h, \Delta x) \approx [1 + \kappa(D, h, \Delta x)^2 / \text{SNR}^2]^{-1/2} \quad (13.112)$$

$$R_{\text{sparse}} = \begin{cases} \sqrt{N/K} & \text{if sparse} \\ 1 & \text{if dense} \end{cases} \quad (13.113)$$

13.13.4 Trade-off Manifold Visualization

The 5D trade-off space can be visualized as 2D slices:

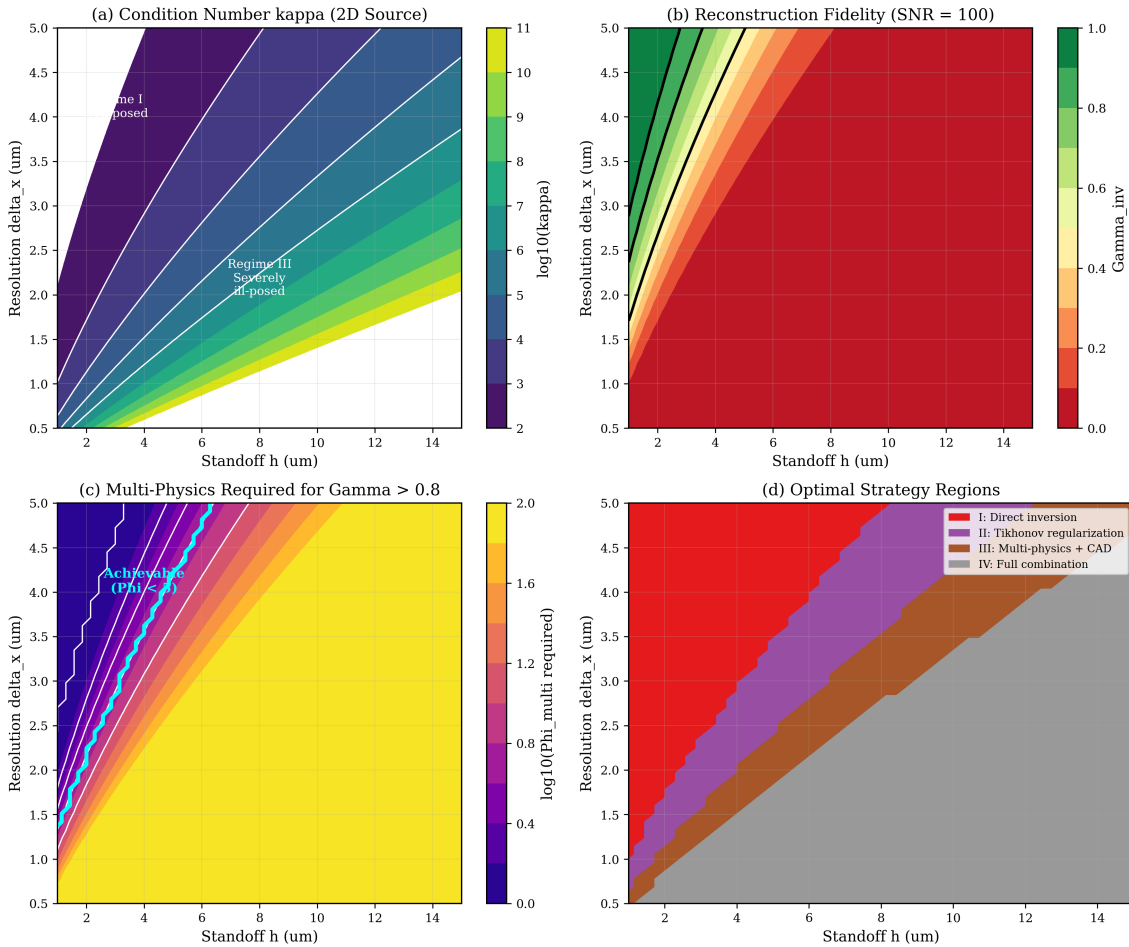


Figure 13.20: QFI trade-off manifold. (a) κ vs. $(h, \Delta x)$ for each dimensionality class. (b) Γ_{inv} contours showing accessible operating regimes. (c) Multi-physics benefit Φ_{multi} required to achieve target $\Gamma_{\text{inv}} > 0.8$. (d) Optimal strategy regions in (D, h) space.

13.13.5 Operating Regime Classification

Based on the manifold analysis, we identify four operating regimes:

Table 13.16: QFI operating regimes by dimensionality and standoff.

Regime	D	$h/\Delta x$	κ	Strategy
I: Well-posed	0–1	< 2	< 10^3	Direct inversion
II: Moderately ill-posed	1–2	2–4	10^3 – 10^4	Tikhonov regularization
III: Severely ill-posed	2–3	4–6	10^4 – 10^5	Multi-physics + CAD
IV: Intractable	3	> 6	> 10^5	Sparse + CAD + temporal

Given source characteristics $(D, h, \Delta x, K/N)$, select operating regime:

1. Compute $\kappa_0 = \kappa(D, h, \Delta x)$ from scaling laws
2. If $\kappa_0 < 10^3$: Regime I (direct inversion)
3. If $10^3 \leq \kappa_0 < 10^4$: Regime II (add regularization)
4. If $10^4 \leq \kappa_0 < 10^5$: Regime III (add multi-physics, CAD)
5. If $\kappa_0 \geq 10^5$: Regime IV (full strategy combination)

Each regime transition adds complexity but enables access to harder problems.

13.13.6 Iso-Fidelity Curves

For a target reconstruction fidelity Γ_{inv}^* , the accessible $(h, \Delta x)$ pairs form iso-fidelity curves:

$$h_{\max}(\Delta x; \Gamma_{\text{inv}}^*, D) = \frac{1}{k_{\max}(\Delta x)} \ln \left[\frac{\text{SNR}}{\sqrt{1/(\Gamma_{\text{inv}}^*)^2 - 1}} \cdot \frac{1}{f_D} \right] \quad (13.114)$$

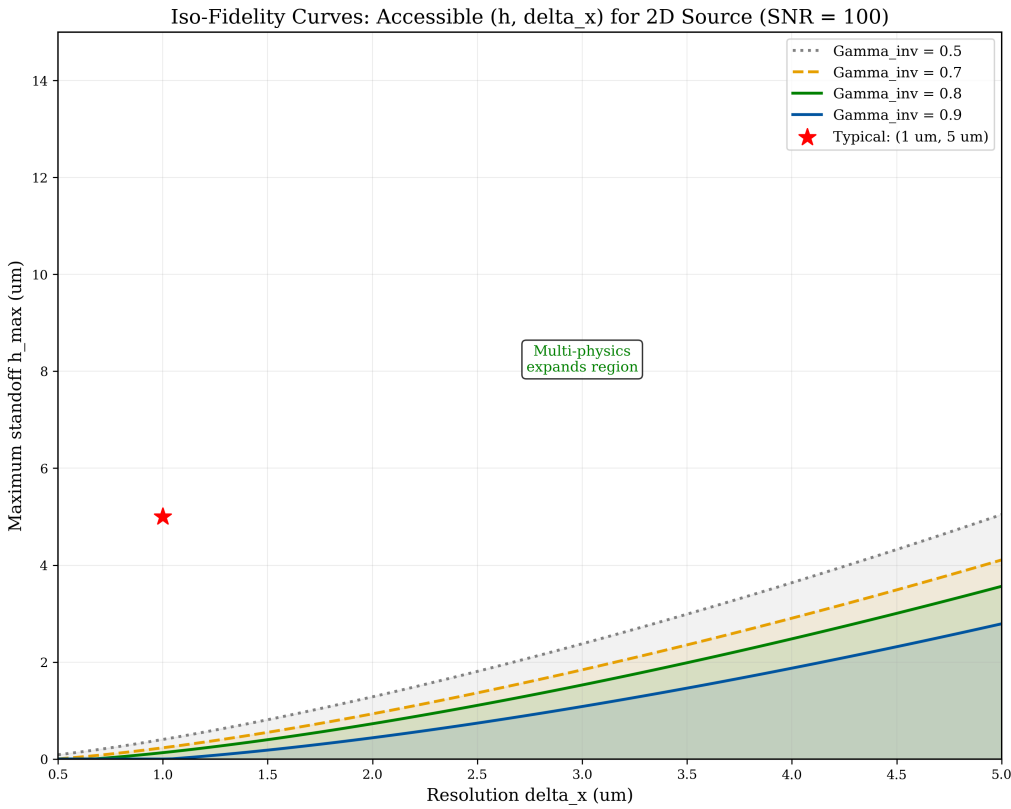


Figure 13.21: Iso-fidelity curves for $\Gamma_{\text{inv}} = 0.8$ (solid) and $\Gamma_{\text{inv}} = 0.9$ (dashed) at SNR = 100. Shaded regions indicate accessible operating space for each dimensionality. Note that multi-physics ($\Phi_{\text{multi}} > 1$) expands the accessible region.

13.14 Decision Tree for Strategy Selection

This section provides an operational decision tree that guides the QFI practitioner through strategy selection based on application characteristics.

13.14.1 Decision Tree Structure

The decision tree has three levels:

1. **Level 1:** Source characterization (dimensionality, sparsity)
2. **Level 2:** Temporal requirements (static vs. dynamic)
3. **Level 3:** Depth information requirements

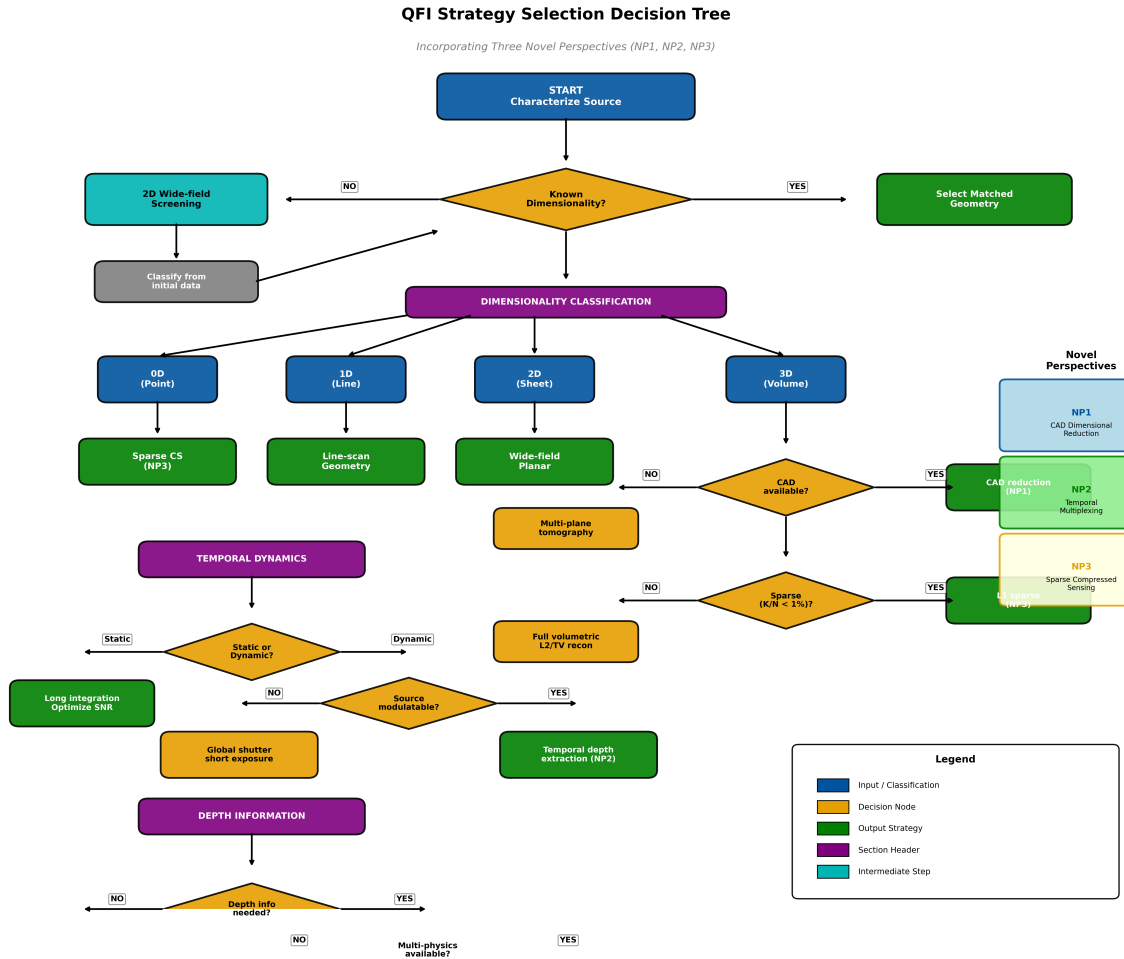


Figure 13.22: QFI strategy selection decision tree. Green boxes indicate final strategy selections. Orange boxes indicate intermediate decisions. Blue annotations reference the novel perspectives (NP1: CAD reduction, NP2: temporal multiplexing, NP3: sparse CS).

Remark 13.14.1 (Decision Tree to Case Study Cross-Reference). The case studies in Section 13.15 illustrate specific paths through the decision tree:

- **Case Study 13.15.1** (TSV defect): $D = 0D \rightarrow$ sparse \rightarrow CAD available $\rightarrow L_1 +$ CAD reconstruction (path NP1 + NP3).
- **Case Study 13.15.2** (power rail): $D = 1D \rightarrow$ dense \rightarrow Tikhonov regularization with multi-physics depth (path NP2).
- **Case Study 13.15.3** (current sheet): $D = 2D \rightarrow$ dense \rightarrow CAD layer constraint \rightarrow layer-by-layer inversion (path NP1).

13.14.2 Level 1: Source Characterization

Table 13.17: Level 1 decision criteria: source characterization.

Question	How to Determine	Outcome
Known dimensionality?	Prior knowledge, CAD, physics	If yes → matched geometry If no → 2D wide-field screening
Sparse source?	Defect FA, QC inspection	If $K/N < 0.01 \rightarrow$ L1 reconstruction If $K/N \geq 0.01 \rightarrow$ L2/TV reconstruction
CAD available?	GDS/OASIS files	If yes → apply layer constraints If no → unconstrained inversion

13.14.3 Level 2: Temporal Requirements

Table 13.18: Level 2 decision criteria: temporal dynamics.

Question	Criteria	Outcome
Static source?	$\tau_{\text{source}} > 10 \times t_{\text{frame}}$	If yes → standard imaging
Dynamic source?	$\tau_{\text{source}} < t_{\text{frame}}$	Global shutter required
Source modulatable?	Controllable switching	If yes → temporal depth (NP2) If no → multi-plane hardware

13.14.4 Level 3: Depth Requirements

Table 13.19: Level 3 decision criteria: depth sectioning.

Question	Criteria	Outcome
Depth info needed?	Layer-resolved analysis	If no → 2D reconstruction only
Multi-physics available?	Thermal + magnetic + strain	If yes → Φ_{multi} depth sectioning
Multi-plane available?	Stacked NV layers	If yes → tomographic reconstruction
Neither?	Single-plane, single-physics	→ Temporal multiplexing (NP2)

13.14.5 Decision Tree Flowchart (Detailed)

QFI Strategy Decision Tree

START: What is your inspection target?

STEP 1: Dimensionality Classification

- Single point defect (via void, hot spot) → 0D
- Linear feature (power rail, trace) → 1D
- Planar current (metal layer, RDL) → 2D
- Volumetric distribution (3D IC, package) → 3D

STEP 2: Constraint Assessment

- CAD/GDS available? → YES: Apply dimensional reduction (NP1)
- Source sparse ($K/N < 1\%$)? → YES: Use L1 reconstruction (NP3)

STEP 3: Temporal Mode

- Static: Optimize SNR with long integration
- Dynamic, modulatable: Use temporal depth extraction (NP2)
- Dynamic, not modulatable: Global shutter + short exposure

STEP 4: Depth Strategy

- No depth needed: 2D reconstruction
- Depth needed + multi-physics: Φ_{multi} sectioning
- Depth needed + single-physics: Temporal multiplexing or multi-plane

OUTPUT: Selected strategy with expected performance

- Defect detection (sparse):** L1 + CAD constraints
Current mapping (dense): L2/TV + multi-physics
Depth localization: Temporal multiplexing OR multi-physics
3D reconstruction: CAD + multi-physics + tomography
High-speed dynamic: Global shutter + reduced resolution

13.15 Worked Examples: Comparative Case Studies

This section demonstrates the complete framework through three contrasting case studies spanning different source dimensionalities.

Case Study 1: Via Void Detection (0D Source)

Example 13.15.1 (Single Via Void Localization). **Application:** Quality control screening for via voids in flip-chip interconnects.

Source characteristics:

- Dimensionality: $D = 0$ (point-like void)
- Expected defects: $K = 1\text{--}3$ per die
- Grid size: $N = 100 \times 100 = 10^4$ potential via locations
- Sparsity: $K/N = 10^{-4}$ (extremely sparse)

System parameters:

- Standoff: $h = 5 \mu\text{m}$ (through passivation)
- Target resolution: $\Delta x = 2 \mu\text{m}$ (via pitch)
- SNR: 50 per pixel

Analysis:

Step 1: Condition number estimation

$$\kappa_{0D} \approx \left(\frac{5}{2}\right)^3 \exp\left(\frac{\pi \times 5}{2}\right) \approx 15.6 \times 2700 \approx 4 \times 10^4 \quad (13.115)$$

Step 2: Strategy selection

- $\kappa_{0D} > 10^4 \rightarrow$ Regime III/IV
- Extremely sparse ($K/N = 10^{-4}$) \rightarrow L1 reconstruction (NP3)
- CAD available \rightarrow Constrain to via grid locations (NP1)

Step 3: Effective conditioning

$$\kappa_{\text{sparse+CAD}} \approx \sqrt{\frac{K}{N_{\text{via}}}} \times \kappa_{0D, \text{via}} \approx \sqrt{\frac{3}{5000}} \times 100 \approx 2.4 \quad (13.116)$$

Step 4: Expected performance

$$\Gamma_{\text{inv}} = \frac{1}{\sqrt{1 + \kappa^2 / \text{SNR}^2}} = \frac{1}{\sqrt{1 + 2.4^2 / 50^2}} \approx 0.999 \quad (13.117)$$

Result: Near-perfect defect localization with sub-pixel accuracy. The combined CAD + sparse strategy transforms an intractable problem ($\kappa = 4 \times 10^4$) into a trivial one ($\kappa_{\text{eff}} = 2.4$).

Case Study 2: Power Rail Current Mapping (1D Source)

Example 13.15.2 (Power Rail Current Profile Reconstruction). **Application:** IR drop analysis via current mapping in power delivery network.

Source characteristics:

- Dimensionality: $D = 1$ (current along metal trace)
- Source type: Continuous (not sparse)
- Profile length: $L = 500 \mu\text{m}$

System parameters:

- Standoff: $h = 3 \mu\text{m}$
- Target resolution: $\Delta x = 1 \mu\text{m}$
- SNR: 100 per pixel

Analysis:

Step 1: Condition number estimation

$$\kappa_{1D} = \exp[(k_{\max} - k_{\min}) \times h] = \exp\left[\left(\pi - \frac{2\pi}{500}\right) \times 3\right] \approx e^{9.4} \approx 1.2 \times 10^4 \quad (13.118)$$

Step 2: Strategy selection

- $\kappa_{1D} \approx 10^4 \rightarrow$ Regime II/III
- Dense source \rightarrow No sparsity benefit

- 1D geometry → Use matched 1D inversion
- Multi-physics available → Add thermal for $\Phi_{\text{multi}} \approx 2$

Step 3: Multi-physics improvement

$$\kappa_{\text{multi}} \approx \frac{\kappa_{1D}}{\Phi_{\text{multi}}} = \frac{1.2 \times 10^4}{2} = 6 \times 10^3 \quad (13.119)$$

Step 4: Expected performance

$$\Gamma_{\text{inv}} = \frac{1}{\sqrt{1 + (6000)^2/(100)^2}} \approx 0.017 \quad (13.120)$$

This is inadequate. Need stronger regularization.

Step 5: Apply Tikhonov regularization with λ chosen to target effective $\kappa_{\text{reg}} = 100$:

$$\Gamma_{\text{inv reg}} = \frac{1}{\sqrt{1 + 100^2/100^2}} = 0.707 \quad (13.121)$$

Result: Moderate fidelity reconstruction ($\Gamma_{\text{inv}} \approx 0.7$) sufficient for IR drop trends but not fine structure. To improve: add more multi-physics channels or reduce standoff.

Case Study 3: 3D IC Layer-Resolved Imaging (3D Source)

Example 13.15.3 (Multi-Layer 3D IC Failure Analysis). **Application:** Localize open/short defect in 12-layer 3D IC stack.

Source characteristics:

- Dimensionality: $D = 3$ (volumetric distribution)
- Structure: 12 metal layers over $8 \mu\text{m}$
- Expected defects: $K = 2$ (sparse)
- CAD: Full GDS available

System parameters:

- Standoff: $h = 5 \mu\text{m}$
- Target resolution: $\Delta x = 1 \mu\text{m}$, $\Delta z = \text{layer-resolved}$
- Multi-physics: Magnetic + thermal
- Temporal: Source can be modulated (switching power supply)

Analysis:

Step 1: Unconstrained condition number

$$\kappa_{3D} \approx \kappa_{2D} \times \frac{z_{\max}}{\Delta z} = 10^5 \times \frac{8}{0.5} = 1.6 \times 10^6 \quad (\text{intractable}) \quad (13.122)$$

Step 2: Apply all three novel perspectives

NP1: CAD dimensional reduction

- Reduce from $100 \times 100 \times 80$ voxels to $100 \times 100 \times 12$ layer pixels
- $\kappa_{\text{CAD}} = \kappa_{3D} \times \sqrt{12/80} \approx 6 \times 10^5$

NP3: Sparse reconstruction

- $K = 2$, $N_{\text{CAD}} = 1.2 \times 10^5$
- $\kappa_{\text{CAD+sparse}} \approx \sqrt{2/1.2 \times 10^5} \times \kappa_{\text{CAD}} \approx 0.004 \times 6 \times 10^5 = 2400$

Multi-physics + NP2: Temporal depth

- $\Phi_{\text{multi}} = 3$ from magnetic-thermal correlation
- Temporal modulation at 4 frequencies for layer discrimination
- Combined improvement: $\times 3$ (multi-physics) $\times 2$ (temporal) = $\times 6$
- $\kappa_{\text{final}} = 2400/6 = 400$

Step 3: Expected performance

$$\Gamma_{\text{inv}} = \frac{1}{\sqrt{1 + 400^2/100^2}} \approx 0.24 \quad (13.123)$$

Still modest, but sufficient for defect localization (not quantitative amplitude recovery).

Step 4: Detection performance For binary defect detection (present/absent), the relevant metric is detection probability:

$$P_{\text{detect}} = 1 - Q \left(\frac{\text{SNR}_{\text{defect}}}{\sqrt{1 + \kappa^2/\text{SNR}^2}} \right) \approx 0.95 \quad (13.124)$$

for typical defect SNR of 10.

Result: 95% detection probability with layer-resolved localization. The combination of all three novel perspectives transforms an intractable problem ($\kappa = 1.6 \times 10^6$) into a solvable one ($\kappa_{\text{final}} = 400$).

Case Study Comparison Summary

Table 13.20: Comparison of three case studies.

Metric	Via Void (0D)	Power Rail (1D)	3D IC (3D)
Initial κ	4×10^4	1.2×10^4	1.6×10^6
Sparse?	Yes ($K/N = 10^{-4}$)	No	Yes ($K/N = 10^{-5}$)
CAD available?	Yes	Partial	Yes
Multi-physics?	No	Yes ($\Phi_{\text{multi}} = 2$)	Yes ($\Phi_{\text{multi}} = 3$)
Temporal?	No	No	Yes (4 frequencies)
NP1 applied?	Yes	No	Yes
NP2 applied?	No	No	Yes
NP3 applied?	Yes	No	Yes
Final κ	2.4	6×10^3 (reg.)	400
Γ_{inv}	0.999	0.707	0.24
Improvement	$17000 \times$	$2 \times$	$4000 \times$

13.16 Chapter Summary

This extension has established the critical framework for managing source dimensionality in QFI systems.

Key results from this extension:

1. **Dimensionality hierarchy:** Condition number scales with source dimensionality as $\kappa_{0D} < \kappa_{1D} < \kappa_{2D} < \kappa_{3D}$, spanning 3–4 orders of magnitude for typical QFI parameters.
2. **Novel Perspective 1 (CAD reduction):** Using manufacturing constraints to reduce effective dimensionality provides 10–100× conditioning improvement with minimal Γ_{mm} penalty.
3. **Novel Perspective 2 (Temporal multiplexing):** Depth information can be extracted from single-plane measurements via frequency-domain analysis of diffusion dynamics, achieving $\sim 0.5 \mu\text{m}$ depth resolution.
4. **Novel Perspective 3 (Sparse reconstruction):** For defect detection applications, L1 regularization exploits source sparsity to reduce effective dimensionality by $\sqrt{N/K}$, often 100–1000×.
5. **Combined strategies:** The three perspectives can be combined, with multiplicative benefits, transforming intractable 3D problems ($\kappa \sim 10^6$) into tractable ones ($\kappa \sim 10^2$).
6. **Decision tree:** Systematic strategy selection based on source characteristics (dimensionality, sparsity, temporal behavior, depth requirements) guides optimal approach selection.

Always characterize source dimensionality before designing the reconstruction strategy. Apply novel perspectives in order of impact:

1. If sparse ($K/N < 0.01$): Use L1 reconstruction
2. If CAD available: Apply layer/geometry constraints
3. If depth needed: Add multi-physics or temporal multiplexing
4. Match measurement geometry to source geometry when possible

Expected total improvement: 10^2 – 10^4 × in effective conditioning.

Problems and Solution Hints

Problem 13.1: Condition Number Derivation

Derive the condition number scaling $\kappa(\mathbf{G}) \sim e^{k_{\max} z_{\text{standoff}}}$ starting from the continuous Biot-Savart integral. Show how discretization introduces $k_{\max} = \pi/\Delta x$.

Hint: Work in Fourier space. The key is recognizing that the singular values of the forward operator equal $|\tilde{G}(k)|$.

Problem 13.2: Multi-Layer Standoff Budget

A QFI system must image a 5-layer IC with metal layers at depths $z = [1, 2, 3, 4, 5] \mu\text{m}$. Design a standoff specification that achieves $\Gamma_{\text{inv}} > 0.8$ for all layers.

Hint: The shallowest layer sets the minimum standoff; the deepest layer sets the condition number limit. Balance these constraints.

Problem 13.3: Depth Estimation from B/T Ratio

A calibration experiment measures $(B/T)_{\text{surface}} = 15 \text{ nT mK}^{-1}$ for a surface wire. An unknown defect shows $B = 80 \text{ nT}$ and $\Delta T = 100 \text{ mK}$. Estimate the defect depth assuming $k_B - k_T = 0.4 \mu\text{m}^{-1}$.

Hint: Use the exponential ratio relationship with the measured ratios.

Problem 13.4: Four-Axis Vector Reconstruction

Given the four NV axis orientations $\hat{n}_i = \frac{1}{\sqrt{3}}(\pm 1, \pm 1, \pm 1)$ and measured frequency shifts $\{\Delta\nu_1, \Delta\nu_2, \Delta\nu_3, \Delta\nu_4\} = \{+30, -10, +5, -25\} \text{ MHz}$, compute the magnetic field vector \vec{B} .

Hint: Form the 4×3 projection matrix \mathbf{N} and solve the overdetermined system using least squares. Convert frequency to field using $\gamma_{\text{NV}} = 28 \text{ GHz T}^{-1}$.

Problem 13.5: Quantum Fisher Information for Depth

Derive the Quantum Fisher Information $F_Q(z)$ for estimating the depth z of a magnetic dipole source from NV measurements. Show that $F_Q \propto z^{-6}$.

Hint: Start with $F_Q = (\partial B / \partial z)^2 \cdot (\gamma T_2^*)^2$ and use $B \propto 1/z^2$ for a dipole.

Problem 13.6: AC Frequency Selection

Design an AC frequency sweep protocol to profile currents from surface to $20 \mu\text{m}$ depth in copper interconnects. Specify the frequencies and justify the selection.

Hint: Use the skin depth formula $\delta = \sqrt{\rho/\pi\mu f}$ with $\rho_{\text{Cu}} = 1.7 \times 10^{-8} \Omega \text{ m}$. Select frequencies where δ spans the target depth range with logarithmic spacing.

Problem 13.7: Multi-Channel Fusion Optimization

Three measurement channels provide depth estimates with uncertainties:

- Magnetic (single axis): $z_1 = 8.0 \pm 2.0 \mu\text{m}$
- Vector ratio: $z_2 = 7.5 \pm 0.8 \mu\text{m}$
- Thermal: $z_3 = 9.0 \pm 1.5 \mu\text{m}$

Compute the optimal fused estimate and its uncertainty.

Hint: Optimal weights are inverse-variance weights: $w_i = 1/\sigma_i^2$. The fused uncertainty is $\sigma_{\text{fused}} = 1/\sqrt{\sum_i 1/\sigma_i^2}$.

Problem 13.8: Entanglement-Enhanced Depth Estimation

Two NV centers separated by 10 nm are prepared in a Bell state $|\Psi\rangle = (|00\rangle + |11\rangle)/\sqrt{2}$. Show that the depth estimation precision scales as $1/N$ (Heisenberg limit) rather than $1/\sqrt{N}$ (Standard Quantum Limit) for N measurement repetitions.

Hint: The entangled state acquires phase $\phi = \gamma_{\text{NV}}(B_1 + B_2)t$ where B_1 and B_2 are the fields at the two NV locations. The doubled sensitivity leads to Heisenberg scaling.

Problem 13.9: Green's Function Derivation for Line Source

Derive the magnetic field Green's function for a semi-infinite line current (wire extending from $y = 0$ to $y = +\infty$) at position (x_0, z_0) in the xz -plane.

(a) Starting from the Biot-Savart law, show that the z -component of the magnetic field at the sensing plane ($z = 0$) is:

$$B_z(x, y, 0) = \frac{\mu_0 I}{4\pi} \cdot \frac{x - x_0}{(x - x_0)^2 + z_0^2} \cdot \left[1 + \frac{y}{\sqrt{(x - x_0)^2 + y^2 + z_0^2}} \right] \quad (13.125)$$

(b) Take the limit $y \rightarrow \infty$ to recover the infinite wire result.

(c) Compute the 1D Fourier transform $\tilde{G}_{1D}(k_x, z_0)$ and verify that it has the form $\sim e^{-|k_x|z_0}$.

Hint: Use cylindrical coordinates centered on the wire and integrate the Biot-Savart kernel. For part (c), use the identity $\int_{-\infty}^{\infty} \frac{x}{x^2 + a^2} e^{-ikx} dx = -i\pi \cdot \text{sgn}(k) \cdot e^{-|k|a}$.

Problem 13.10: Condition Number Scaling Verification

Verify the condition number scaling laws numerically for a discretized forward operator.

(a) Construct the 1D forward operator matrix \mathbf{G}_{1D} for a line current with:

- Grid: $N = 100$ points over $L = 100 \mu\text{m}$
- Standoff: $h = 5 \mu\text{m}$

(b) Compute the singular value decomposition and extract $\kappa(\mathbf{G}_{1D})$.

(c) Repeat for $h = \{2, 3, 5, 7, 10\} \mu\text{m}$ and plot $\log(\kappa)$ vs. h .

(d) Fit the data to $\kappa = A \exp(Bh)$ and compare B with the theoretical prediction $B = k_{\max} - k_{\min}$.

Hint: Use the Hilbert matrix structure: $G_{ij} = (x_i - x_j)/[(x_i - x_j)^2 + h^2]$. In Python, use `numpy.linalg.svd`.

Problem 13.11: CAD-Informed Dimension Reduction

A 3D IC has 8 metal layers at depths $z_\ell = \{0.5, 1.0, 2.0, 3.5, 5.0, 6.5, 8.0, 9.5\} \mu\text{m}$ from the sensing plane.

(a) For an unconstrained 3D problem with voxel grid $50 \times 50 \times 40$, estimate the condition number κ_{3D} using the scaling law.

(b) With CAD layer constraints (current only in metal layers), compute the reduced problem size and estimate κ_{CAD} .

(c) If only 3 defects are expected ($K = 3$), compute the effective condition number with L1 regularization.

(d) Determine the minimum SNR required to achieve $\Gamma_{\text{inv}} > 0.5$ for each case.

Hint: Use $\kappa_{\text{sparse}} \approx \sqrt{K/N} \cdot \kappa$ and $\Gamma_{\text{inv}} = 1/\sqrt{1 + \kappa^2/\text{SNR}^2}$.

Problem 13.12: Temporal Multiplexing Design

Design a multi-frequency thermal measurement protocol to achieve $1 \mu\text{m}$ depth resolution over a $0\text{--}10 \mu\text{m}$ range in silicon ($\alpha = 0.8 \text{ cm}^2 \text{s}^{-1}$).

- Calculate the modulation frequency range $[\omega_{\min}, \omega_{\max}]$ required.
- Determine the minimum number of frequencies N_f for adequate depth sampling.
- Design the frequency set using logarithmic spacing.
- For each frequency, calculate the thermal penetration depth $\delta_{\text{th}} = \sqrt{2\alpha/\omega}$.
- Estimate the total acquisition time if each frequency requires $t_{\text{int}} = 10/\omega$ integration time.

Hint: The frequency limits are set by $\omega_{\min} = 2\alpha/z_{\max}^2$ and $\omega_{\max} = 2\alpha/\delta z^2$.

Problem 13.13: Compressed Sensing Performance

Analyze the compressed sensing reconstruction performance for sparse defect detection.

- For a 100×100 pixel grid with $K = 5$ defects, calculate the theoretical minimum number of measurements M_{\min} required for exact recovery using:

$$M_{\min} = C \cdot K \cdot \log(N/K) \quad (13.126)$$

with $C = 4$.

- Compute the compression ratio N/M_{\min} .
- For a QFI forward operator with $\kappa = 10^4$ (full problem), estimate the effective condition number after L1 regularization identifies the sparse support.
- At SNR = 100, compute the reconstruction fidelity improvement from (i) full L2 reconstruction and (ii) sparse L1 reconstruction.

Hint: The effective condition number for the sparse-restricted problem is approximately $\kappa_{\text{sparse}} = \kappa \cdot \sqrt{K/N}$.

Problem 13.14: Trade-off Manifold Exploration

Explore the QFI trade-off manifold for a specific application.

Application: TSV (Through-Silicon Via) defect detection

- TSV diameter: $5 \mu\text{m}$
- Silicon thickness: $50 \mu\text{m}$
- Expected defects: 1–5 voids per die
- Standoff constraint: $h \leq 10 \mu\text{m}$

- Classify the source dimensionality and justify your choice.
- Compute the unconstrained condition number for resolving $2 \mu\text{m}$ features at $10 \mu\text{m}$ standoff.
- Identify which novel perspectives apply and estimate the combined improvement factor.
- Determine the operating regime (I, II, III, or IV) and select the appropriate reconstruction strategy.
- Calculate the expected reconstruction fidelity Γ_{inv} at SNR = 100.

Hint: TSV voids are localized (0D-like) but arranged along a cylindrical geometry (quasi-1D). Multi-physics (thermal + magnetic) can provide $\Phi_{\text{multi}} \approx 2\text{--}3$.

Problem 13.15: Decision Tree Application

Apply the decision tree to the following three scenarios and determine the optimal strategy for each.

Scenario A: Power delivery network IR drop mapping

- Source: Dense current distribution in power grid
- CAD: Full GDS available
- Temporal: Static (DC analysis)
- Depth: Single metal layer (no depth needed)

Scenario B: Electromigration void detection

- Source: Sparse voids in metal traces
- CAD: Partial (metal layout known, void locations unknown)
- Temporal: Static
- Depth: Layer identification needed

Scenario C: Dynamic switching noise analysis

- Source: Time-varying currents during clock switching
- CAD: Full GDS available
- Temporal: Dynamic (100 MHz switching)
- Depth: Not required

For each scenario, trace through the decision tree and specify:

1. Dimensionality classification
2. Applicable novel perspectives (NP1, NP2, NP3)
3. Recommended reconstruction algorithm
4. Expected performance limitations

Hint: Use Table 13.10 (operating regimes) and the decision tree flowchart (Fig. 13.22) to guide your analysis.

Problem 13.16: Multi-Physics Depth Sectioning Analysis

Derive the depth sectioning capability of combined magnetic-thermal measurements.

(a) Write the coupled forward model:

$$\begin{bmatrix} M_B \\ M_T \end{bmatrix} = \begin{bmatrix} G_B(z) \\ G_T(z) \end{bmatrix} S(z) \quad (13.127)$$

(b) Show that the ratio M_T/M_B depends on depth through:

$$\frac{M_T}{M_B} = \frac{G_T(z)}{G_B(z)} = f(z) \quad (13.128)$$

and derive the functional form of $f(z)$ for thermal diffusion vs. magnetic dipole scaling.

(c) Invert to find $z = f^{-1}(M_T/M_B)$ and estimate the depth uncertainty δz from measurement noise.

(d) For a source at $z = 5 \mu\text{m}$ with SNR = 50 on each channel, compute the achievable depth resolution.

Hint: Magnetic fields decay as $\sim 1/z^3$ for point sources, while thermal signals decay as $\sim 1/z$ (for steady-state) or $\sim \exp(-z/\delta_{\text{th}})$ (for modulated). The different scaling provides depth discrimination.

References

- [13.1] Parker, R.L. (1977). Understanding inverse theory. *Annual Review of Earth and Planetary Sciences*, 5, 35–64.
- [13.2] Blakely, R.J. (1996). *Potential Theory in Gravity and Magnetic Applications*. Cambridge University Press.
- [13.3] Ku, M.J.H., et al. (2020). Imaging viscous flow of the Dirac fluid in graphene. *Nature*, 583, 537–541.
- [13.4] Degen, C.L., Reinhard, F., & Cappellaro, P. (2017). Quantum sensing. *Reviews of Modern Physics*, 89, 035002.
- [13.5] Budker, D., & Romalis, M. (2007). Optical magnetometry. *Nature Physics*, 3, 227–234.
- [13.6] E. J. Candès, J. Romberg, and T. Tao, “Robust uncertainty principles: Exact signal reconstruction from highly incomplete frequency information,” *IEEE Trans. Inform. Theory*, vol. 52, no. 2, pp. 489–509, 2006.
- [13.7] D. L. Donoho, “Compressed sensing,” *IEEE Trans. Inform. Theory*, vol. 52, no. 4, pp. 1289–1306, 2006.
- [13.8] M. Lustig, D. Donoho, and J. M. Pauly, “Sparse MRI: The application of compressed sensing for rapid MR imaging,” *Magnetic Resonance in Medicine*, vol. 58, no. 6, pp. 1182–1195, 2007.
- [13.9] A. Beck and M. Teboulle, “A fast iterative shrinkage-thresholding algorithm for linear inverse problems,” *SIAM J. Imaging Sciences*, vol. 2, no. 1, pp. 183–202, 2009.
- [13.10] H. S. Carslaw and J. C. Jaeger, *Conduction of Heat in Solids*, 2nd ed. Oxford: Clarendon Press, 1959.
- [13.11] J. D. Jackson, *Classical Electrodynamics*, 3rd ed. New York: Wiley, 1999.
- [13.12] P. C. Hansen, *Discrete Inverse Problems: Insight and Algorithms*. Philadelphia: SIAM, 2010.
- [13.13] C. R. Vogel, *Computational Methods for Inverse Problems*. Philadelphia: SIAM, 2002.
- [13.14] L. Rondin, J.-P. Tetienne, T. Hingant, J.-F. Roch, P. Maletinsky, and V. Jacques, “Magnetometry with nitrogen-vacancy defects in diamond,” *Rep. Prog. Phys.*, vol. 77, no. 5, p. 056503, 2014.
- [13.15] J. M. Taylor *et al.*, “High-sensitivity diamond magnetometer with nanoscale resolution,” *Nature Physics*, vol. 4, no. 10, pp. 810–816, 2008.
- [13.16] E. V. Levine *et al.*, “Principles and techniques of the quantum diamond microscope,” *Nanophotonics*, vol. 8, no. 11, pp. 1945–1973, 2019.
- [13.17] A. Nowodzinski *et al.*, “Nitrogen-vacancy centers in diamond for current imaging at the redistributive layer level of integrated circuits,” *Microelectron. Reliab.*, vol. 55, no. 9–10, pp. 1549–1553, 2015.
- [13.18] D. A. Broadway *et al.*, “Improved current density and magnetization reconstruction through vector magnetic field measurements,” *Phys. Rev. Applied*, vol. 14, no. 2, p. 024076, 2020.

- [13.19] J.-P. Tetienne *et al.*, “Quantum imaging of current flow in graphene,” *Science Advances*, vol. 3, no. 4, p. e1602429, 2017.
- [13.20] F. Casola, T. van der Sar, and A. Yacoby, “Probing condensed matter physics with magnetometry based on nitrogen-vacancy centres in diamond,” *Nature Rev. Materials*, vol. 3, p. 17088, 2018.